Numerical and experimental investigations of the early injection process of Spray G in a constant volume chamber and an optically accessible DISI engine

Andrea Pati[1] (ID)**, Davide Paredi[2]** (ID)**, Cooper Welch[3]** (ID)**, Marius Schmidt[3]** (ID)**, Christopher Geschwindner[3]** (ID)**, Benjamin Böhm[3], Tommaso Lucchini[2]** (ID)**, Gianluca D'Errico[2]** (ID) **and Christian Hasse[1]** (ID)

Abstract

In this work, the Engine Combustion Network Spray G injector was mounted in the Darmstadt optical-accessible engine to study phenomena typical of multi-hole, early direct-injection events in spark-ignition engines characterized by tumble flow charge motion. Dedicated experimental measurements of both in-cylinder spray morphology and flow velocities before and after the injection process were carried out to assess the adopted numerical setup under real engine conditions. A dynamic secondary breakup model from the literature was coupled with an atomization multi-motion regime model. The model was validated against state-of-the-art ECN Spray G experiments for a constant-volume chamber under low evaporating condition. Then, the simulation of the spray injection in the engine was carried out and the achieved results were compared against the experimental data. Overall, good agreement between experiments and simulations was observed for the spray morphology and velocity fields in both cases. With reference to engine calculations the intake flow was seen to induce spray asymmetry. A partial vortex generated during the intake phase on the tumble plane interacts with the spray, developing into a full vortex which induces an upward flow that stabilizes the spray. The upward flows below the intake valve increase the dilution of the plume outside the tumble plane, which therefore exhibits reduced penetration. Moreover, the intake valves protect from the energetic intake flow the recirculation vortex generated at the tip of the plumes that lie outside the tumble plane. The intake flow helps fuse the vapor fuel clouds of the individual plumes near the injector tip, obtaining a vapor fuel with a shape like that generated by a horseshoe multi-hole injector. Finally, a phenomenological model of the interaction between the multi-hole injector jets and the engine intake flow was introduced to describe the spray evolution in a typical DISI engine.

Introduction

Direct-injection spark-ignition (DISI) engines are nowadays widely used to reduce CO_2 emissions due to their propensity to work with stratified and globally lean mixtures.[1] Further, homogeneous fuel-air charges are still used in high-speed and high-load operating conditions.[2]

In the first implementations of DISI engines, the spray was redirected near the spark plug by the piston and the cylinder head walls,[3] with a geometry better known as a *wall-guided* configuration. Further, swirl injection was widely used.

[1]Department of Mechanical Engineering, Simulation of reactive Thermo-Fluid Systems, Technical University of Darmstadt, Darmstadt, Germany
[2]Department of Energy, Internal Combustion Engines Group, Politecnico di Milano, Milano, Italy
[3]Department of Mechanical Engineering, Reactive Flows and Diagnostics, Technical University of Darmstadt, Darmstadt, Germany

Corresponding author:
Andrea Pati, Department of Mechanical Engineering, Simulation of reactive Thermo-Fluid Systems, Technical University of Darmstadt, Otto-Berndt-Str. 2, Darmstadt 64287, Germany.
Email: pati@stfs.tu-darmstadt.de

Nowadays *spray-guided* configurations are preferred, where the spray itself is designed to provide the proper atomization and mixing, reducing wall-wetting, and the subsequent formation of soot.[1,4]

The position of the injector and the interaction of the spray with the airflow have been extensively reviewed and investigated in both experimental and numerical studies.[1] Han et al.[5,6] carried out numerical investigation on a centrally mounted swirl injector in an engine with tumble intake. They observed that the cross-flow generated by the intake flow deflects the spray, increasing its penetration and leading to spray impinging on the cylinder wall. This conclusion has also been confirmed with experimental research,[7] and with different geometries.[8]

Alexander et al.[9] investigated a tumble engine with a side-mounted swirl injector. It was observed that the spray is swept by the co-axial flow generated by the intake flow, which tends to flatten the spray and to constrain it toward its centerline. The authors also suggested that can be difficult to infer spray behavior by observing only a single plane.

Yi et al.[10] investigated a similar geometry but with forward tumble intake flow. A strong reduction in the spray angle was observed. Moreover, the spray was reported to bend toward the injection location. This bend was responsible for hindering the spray penetration, evaporation, and fuel-air mixing homogeneity.

Swirl injectors are not suitable in *spray-guided* configurations because the spray evolution strongly depends on the ambient conditions and its tendency to collapse which worsens the air-fuel mixing.[11] For this reason, multi-hole injectors have been incorporated into recent spray-guided DISI engines due to their good stability, which does not depend on the injection timing,[12] and their ability to achieve stratification.[13]

Multi-hole injectors were widely studied in constant-volume chambers (CVCs). The spray is injected into a static, closed environment allowing its evolution to be investigated with different environments and injector geometries. These studies have proven that opening angles are almost independent of the ambient pressure compared to swirl atomizers.[11]

In the engines, multi-hole injectors show reduced hydrocarbon (HC) emissions and reduced sensitivity to the in-cylinder flow field conditions.[14] Notwithstanding this, the in-cylinder airflow is an essential factor in the formation of the fuel-air mixture. As an example, a swirl motion improves mixture homogeneity while a tumble motion induces stratification.[14,15]

Air entrainment in a multi-hole spray is governed by axial and radial airflows. Inter-plume interaction affects the air entrainment and consequently mixture formation and fuel cloud coherency, defined as the contiguity of the fuel vapor region generated by evaporation of multiple plumes (as opposed to the formation of separated fuel vapor regions due to the evaporation of individual plumes).[16]

Previous works observed that the spray evolution in the engine during early injection differs from what is found in a CVC. Engine speed increases strong plume interactions, the loss of distinct plume structures and increased evaporation, mainly caused by the in-cylinder velocities induced by the piston downward speed.[17]

Geschwindner et al.[18] have studied the Engine Combustion Network (ECN) Spray G inside an optically accessible engine during the compression phase. They have shown that the reduction in the spray angle during the injection is slowed down by the in-cylinder flow directed toward the spray and the higher axial air entrainment induced by the piston's upward motion. The in-cylinder flow therefore plays a relevant role in spray stabilization and plume-plume interactions.

Conversely, the momentum injected by multi-hole injector sprays has an influence on the flow field and specifically on the tumble motion inside the cylinder. Right after the injection, vortices are generated at the tip of the plumes influencing the air entrainment.[19] In the case of late injections, the destruction of the tumble motion after the injection has been observed.[18] On the other hand, the tumble motion can be energized in the case of early injection by the momentum induced by the spray if the injector arrangement is favorable.[20]

Computational fluid dynamics (CFD) constitutes a powerful diagnostic tool to study the spray evolution in a DISI engine environment. Lagrangian–Eulerian approaches are suitable for investigating spray evolution when coupled with a breakup model such as the Kelvin–Helmholtz Rayleigh–Taylor (KHRT) model, if the parameter are adjusted.[21,22] Spray sub-models have been continuously improved over the years, aiming to increase their accuracy for a broader range of operating conditions while minimizing the set of parameters to be calibrated and adjusted by the user.[23] However, the prediction of the spray evolution in simulations still represents an ongoing challenge[24] as it is an event which is strongly influenced by the flow field induced by the spray itself.[25]

The Engine Combustion Network (ECN) Spray G injector is a well-known, extensively validated and widely used multi-hole research injector characterized by a wide range of physical phenomena which are typical of different engine operating points.[26] In this work the Spray G geometry was coupled with the Darmstadt optically accessible research engine and investigated both experimentally and numerically. First, in the section on the "Engine and Injector Setup," engine and injector geometries are introduced. Furthermore, the coordinate system and the definitions of morphological parameters are introduced.

In the section on the "Spray Model," the Lagrangian method employed for the spray simulations is described. In further detail, there is a specific focus on describing the adopted spray approach which employs a literature-based, dynamic KHRT mechanism for secondary breakup, and an adapted multi-motion regime methodology for modeling the primary atomization of

the spray. The main scope of the proposed approach is to provide a valid methodology for modeling complex low-evaporating sprays for DISI engines while minimizing the parameter adjustments and model adjustment required from the user.

Subsequently, in the section on the "Experimental Setup," the experimental setup of the engine coupled with the Spray G and the tested operating conditions are illustrated. The post-processing procedures which were used to derive the in-engine spray morphology and velocity fields are then outlined.

In the section on the "Numerical Simulation Setup," the overall numerical methodology is explained. In the subsection "Constant-Volume Chamber Configuration," a simulation of the ECN Spray G3 under CVC condition is analyzed and the main parameters that are employed to validate the proposed model are introduced. The subsection "Engine Configuration" describes the numerical setup which was adopted to simulate the motored engine coupled with the Spray G injector geometry. Additionally, a post-processing algorithm is developed and employed to ensure that the comparison with the experimental measurements performed on the engine is consistent.

Specifically, the results are presented as follows. In the section entitled "Results: Spray in Constant-Volume Chamber," results from the CVC simulation are presented with a preliminary validation of the proposed spray model. Then, in the section "Results: Spray in Engine," both experimental and numerical results achieved for the motored engine combined with the Spray G injector are presented. The focus is on the morphology of the spray's liquid phase and on the analysis of the flow velocities on the tumble plane. Therefore, the experimental and numerical velocity fields before and after the injection are compared on the tumble plane with the aim of assessing the global impact of the phenomenon on the gas velocity.

Moreover, the spray evolution and mixture formation are further investigated by exploiting the potential of the CFD. Specifically, four different planes are analyzed focusing on the intake flow, valve, and inter-plume interactions. Finally, conclusions are drawn and conceptual models are introduced and discussed to understand the main aspects related to the spray evolution in an engine which is characterized by an intake tumble motion.

Engine and injector setup

The Darmstadt engine is a well-characterized, four-valve, single-cylinder spark-ignition optical research engine equipped with a pent-roof cylinder head, a fused-silica cylinder liner, and a flat piston window stemming from a Bowditch extension for optical access.[27] A multi-hole Spray G injector, manufactured by Delphi and widely investigated in the ECN community, was installed to carry out the experimental and numerical investigations presented in this work.
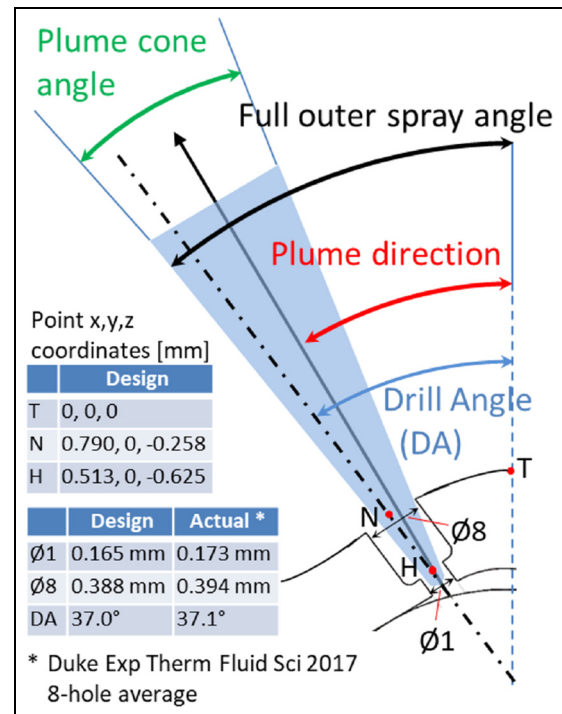

Figure 1. ECN conventions and Spray G injector specifications.[28]

Reference geometric characteristics of the injector and the main ECN conventions are reported in Figure 1.

In this work, the Spray G was numerically modeled according to the design specifications provided by the ECN.[24,28] The adopted geometry is characterized by eight holes evenly spaced in a circular pattern, an orifice drill angle of 37°, an orifice length/diameter ratio of 1.4, a bend angle equal to 0°, and a nominal orifice diameter of 0.165 mm. The employed rate-of-injection profile was measured with a tube method at General Motors.[29] The reference injection pressure is equal to 20 MPa, with a nominal injected fuel mass of 10 mg.

Under CVC conditions, there are several operating points which are well-defined by the ECN.[29] In this work, the focus was on the operating point "G3 – Early Injection," a low-evaporating configuration typical of early injection events in GDI engines operating at full load and characterized by the absence of flash boiling when iso-octane is used as fuel. A constant-volume chamber ambient pressure of 100 kPa, an ambient temperature of 333.15 K, and a fuel temperature equal to 363.15 K define the static vessel G3 setup.

A schematic of the engine cylinder is displayed in Figure 2. A representative example of the spray is shown in Figure 3, where the mounting angle of 8° is highlighted and the measured spray parameters quantities are visible. Additionally, Figure 4 shows a schematic of the planes used to sample the flow field and the vapor fuel field in engine simulations.

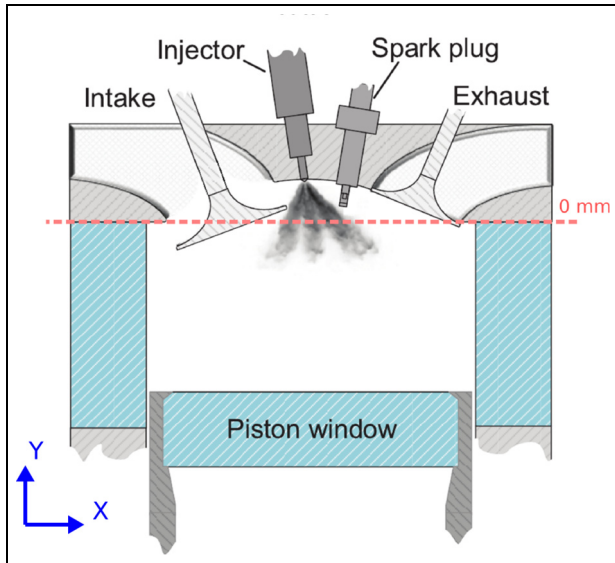The spray angle is defined in Figure 3 using equation (1):

Figure 2. Configuration of the Darmstadt Engine coupled with the ECN injector Spray G; a raw Mie image is superimposed on the sketch for the sake of clarity; the global coordinate system is visible in the corner and the red dashed line identifies the zero *y*-coordinate. This figure was derived from Geschwindner et al.[18]
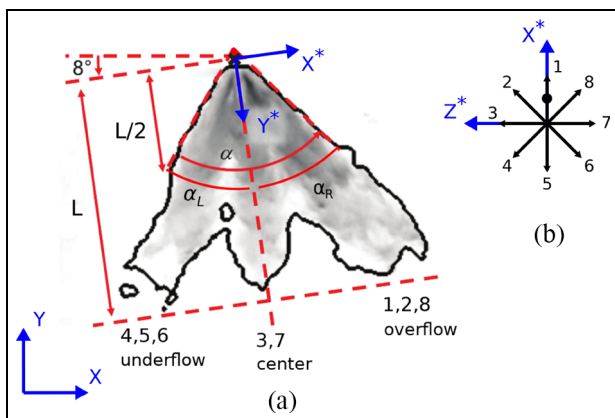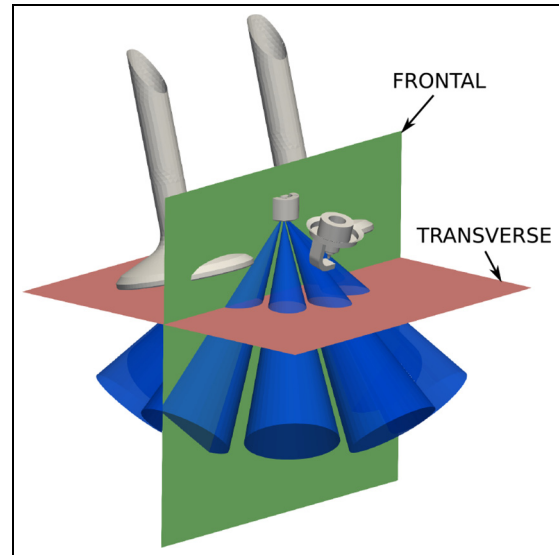

Figure 4. Definition of the sample planes to study the interaction of the plumes and the intake flow. The intake valves, spark plug, and injector are shown in gray. Plumes are visible in blue. The frontal plane $x^* = 0$ mm is shown in green. The transverse plane $y^* = 15$ mm is shown in red. The transverse plane $y^* = 30$ mm and the tumble plane $z^* = 0$ mm are not shown for the sake of clarity.

Figure 3. (a) Local coordinate system for spray studies in the engine; the angles and penetration length are shown for reference and (b) plume enumeration; the dot identifies the plume oriented toward the spark plug. The image is derived from the work of Geschwindner et al.[18]

$$\alpha = \alpha_L + \alpha_R \qquad (1)$$

while the asymmetry factor is defined in equation (2):

$$F_a = \frac{\alpha_R}{\alpha_L} \qquad (2)$$

The axial penetration L is related to the local coordinate axis y^*.

Spray model

An Eulerian-Lagrangian approach[30] was employed to describe the spray evolution for both vessel and engine simulations. Within this context, a Lagrangian liquid column of fuel leaves the injector nozzle and it is then subjected to atomization, secondary breakup, drag, and evaporation phenomena which are numerically described by means of suitable sub-models.

The parcels were injected into the computational domain with a blob-injector mechanism. This involves the parcel being injected with a diameter corresponding to the nozzle diameter and a velocity value increased by a coefficient $\frac{1}{C_d}$, with C_d set equal to 0.73 according to previous experimental findings on the Spray G injector.[31]

To minimize the number of adjustable parameters, a unified spray model was adopted in this work to describe both atomization and secondary breakup phenomena.[32] The secondary breakup phase was managed using an approach developed by Nagaoka and Kawamura[33] and based on the classic KHRT method[21] (competing *catastrophic* Rayleigh–Taylor (RT) and *wave* Kelvin–Helmholtz (KH) mechanisms), which was investigated and incorporated into the adopted numerical framework. The atomization phase was modeled by means of the Pilch–Erdman multi-motion regime approach.[34]

It is reported in the literature[35] that the stripping KH mechanism may be applied to atomize the drops in the liquid core region of the spray. However, for the Spray G1 condition, it was observed that the stripping of child parcels could lead to an overestimation of the droplet diameter decrease near the injector nozzle if not carefully controlled.[36] The small parcels are then carried by the injection momentum without evolving any further, negatively affecting both the spray morphology

and the air entrainment near the nozzle as their interaction with the surrounding gas becomes negligible. As a consequence, the multi-motion regime mechanism proposed by Pilch and Erdman[34] was chosen to model the atomization phase of GDI sprays. This is because previously reported results demonstrated an improvement both regarding the spray morphology near the injector nozzle and the prediction of the centerline gas velocity.[32,36]

In this work, an approach of this kind was integrated into a unified numerical model, permitting direct interaction with the dynamic secondary breakup mechanism. To automatically distinguish between atomization and secondary breakup zones a core length threshold is defined using equation (3)[35]

$$L_c = C \cdot D_{nozzle} \sqrt{\frac{\rho_l}{\rho_g}} \qquad (3)$$

where C expresses the influence of the nozzle flow conditions, D_{nozzle} is the nozzle diameter, and ρ_l and ρ_g respectively represent the liquid and ambient gas densities.

With reference to the KHRT[21] secondary breakup model, the RT mechanism defines the fastest growing wavelength Λ_{RT} according to equation (4):

$$\Lambda_{RT} = 2\pi C_{RT} \sqrt{\frac{3\sigma}{a(\rho_l - \rho_g)}} \qquad (4)$$

The term σ stands for the liquid fuel surface tension. The term a is the acceleration of the drop (equation (5)), which depends on the liquid and gas densities (ρ_l and ρ_g), the liquid-gas relative velocity U_{rel}, the parcel diameter D, and the droplet drag coefficient C_D, as described in equation (5)

$$a = \frac{3}{4} C_D \frac{\rho_g U_{rel}^2}{\rho_l D} \qquad (5)$$

The RT mechanism does not strip child drops from the parent parcels. The diameter reduction of the primary droplet is carried out by means of a catastrophic breakup which occurs when the drop RT distortion time is equal to or greater than the characteristic RT breakup time τ_{RT}. The new diameter of the parcel is assumed to be equal to Λ_{RT}.

The model parameter C_{RT} can be adjusted to match experimental data. A larger value leads to a larger wavelength, making the condition on RT distortions less likely to be satisfied for a specific parcel, thus reducing the probability of catastrophic breakup.

In the classic model formulation, C_{RT} represents a fixed constant which is specifically set for each spray case. This may prove to be a limiting factor because continuous recalibrations could be required when the physical characteristics of the simulated operating points change considerably.

This aspect becomes particularly evident in the case of low-evaporating GDI sprays such as ECN G3, which is characterized by atmospheric ambient pressure, low ambient density, and a reduced Weber gas number (We_g), defined using equation (6):

$$We_g = \frac{\rho_g U_{rel}^2 (D/2)}{\sigma} \qquad (6)$$

That is, the Weber gas number may fall considerably below the values typical of the catastrophic breakup regime[34] reducing the efficiency of the RT mechanism. As a consequence, significant tuning of the C_{RT} parameter could be required to force the RT approach to consistently model the secondary breakup process.

In this work, the approach developed by Nagaoka and Kawamura[33] was employed, as mentioned above. The C_{RT} parameter is described by equation (7)

$$C_{RT} = \max(1.0, 0.11\sqrt{We_g}) \qquad (7)$$

C_{RT} is seen to increase with We_g and relatively high values could also be obtained from parcel with small Weber gas numbers. This condition appears to be suitable for modeling low-evaporating sprays because it tends to minimize the impact of the RT mechanism on the overall secondary breakup process. Physically, this behavior would correspond to a spray with a low Weber gas number, where a catastrophic breakup is less likely to be observed.

Overall, Nagaoka and Kawamura developed an approach which ensured there was a consistent breakup mechanism for droplets both within plumes and under isolated conditions. As a consequence, the main KH B_0 and B_1 model parameters are also not treated like static constants but vary according to the most relevant physical characteristics of the parcels.[33] This assumption should allow both catastrophic and shear breakup times to be consistent with the total breakup time correlation proposed by Pilch and Erdman[34] and Nagaoka and Kawamura[33] while ensuring that a spray model is capable of managing secondary child parcels stripping.

B_0 and B_1 are thus respectively described by equations (8) and (9),[33] while parent parcels are characterized by a reduction in their diameter which is expressed by equation (10)

$$B_0 = 0.61 \left[1.0 - 1.43 \left(\frac{\rho_g}{\rho_l} \right)^{0.2} exp\left(\frac{-We_g}{10} \right) \right] \qquad (8)$$

$$B_1 = 161.7 \sqrt{\frac{\rho_g}{\rho_l}} min \left[1.0, \left(\frac{15}{We_g} \right)^{0.8} \right] \qquad (9)$$

$$\frac{dD}{dt} = -\frac{D - D_{KH}}{\tau_{KH}} \qquad (10)$$

where τ_{KH} is the shear breakup time (equation (11)) function both of Ω_{KH} and the characteristic wavelength Λ_{KH} whose effect is suitably calibrated by means of the specific B_1 model constant.

$$\tau_{KH} = \frac{3.788 B_1 (D/2)}{\Omega_{KH} \Lambda_{KH}} \qquad (11)$$

Table 1. Main spray model parameters.

Atomization	Pilch–Erdman
Breakup	Nagaoka–Kawamura KHRT
Heat transfer	Ranz–Marshall[37,38]
C_{RT}	Dynamic with equation (7)
B_0	Dynamic with equation (8)
B_1	Dynamic with equation (9)
$C_{1,\varepsilon}$	1.55
Plume cone angle	22°
Drill angle	37°

Table 2. Darmstadt engine and in-engine spray parameters.

Average intake pressure	95 kPa
Engine speed	800 rpm
Electronic start of injection (ESOI)	270° beforeTDC
Electronic pulse duration	0.680 ms
Hydraulic delay	307 μs
Injector angle	8°
Fuel	Iso-octane
Fuel pressure	20 MPa
Fuel temperature	333.15 K
Fuel mass	10 mg
Bulk gas	Air
Bulk gas relative humidity	1.8%
Intake temperature	310.15 K
Bulk gas density	1.07 kg/m^3

The term D_{KH} represents the child droplet diameter which is proportional to Λ_{KH} by means of the B_0 model parameter (equation (12)).

$$D_{KH} = 2B_0\Lambda_{KH} \tag{12}$$

A mass-based approach[35] was used to model the liquid evaporation with equation (13)

$$\dot{m}_d = \pi D\beta\rho_v Sh \ln\left(\frac{1-Y_{v,\infty}}{1-Y_{v,s}}\right) \tag{13}$$

where β is the mass diffusion coefficient, ρ_v is the density of the vapor fuel, Sh represents the Sherwood number, and $Y_{v,s}$ and $Y_{v,\infty}$ are the fuel mass fractions respectively under saturation conditions and in the gas phase far away from the droplet surface.

The main specifications of the adopted numerical setup are summarized in Table 1.

Experimental setup

Experimental engine parameters

Spray experiments on the Darmstadt engine were conducted using a spray-guided cylinder head configuration with a compression ratio of 8.7:1. Details on the engine test bench are given by Baum et al.[27] and the spray-guided cylinder head details are presented by Frudenhammer et al.[39] To match the ECN guidelines of "G3 – Early Injection" and to be consistent with the standard operating conditions of the Darmstadt engine as previously reported in the literature, an intake pressure of 95 kPa, an engine speed of 800 rpm, and an injection timing of 270° beforeTDC were selected. A summary of relevant engine and spray parameters is shown in Table 2.

Spray visualization and in-cylinder flow measurements

Engine spray visualization and in-cylinder flow measurements were achieved non-simultaneously via bottom-illuminated Mie scattering and high-speed particle image velocimetry (PIV), respectively.

Mie scattering. Using the operating conditions outlined in Table 2, 100 consecutive cycles of spray images were acquired via Mie scattering. For the optical arrangement, a green-light (525 nm) LED system (ILA 5150 GmbH) equipped with a 40 mm aspherical condenser lens provided volumetric illumination via the piston mirror assembly, and a high-speed CMOS camera (Phantom v711, Vision Research) equipped with a Nikon lens (50 mm, f/5.6) acquired images at a repetition rate of 16 kHz. For a diagram of the Mie scattering setup used in this study, see Figure 4 of Geschwindner et al.[18]

As detailed in Geschwindner et al.,[18] the post-processing of the Mie scatter images consisted of three main stages: first, masking was applied to eliminate reflective engine components; second, background subtraction using the first three dark frames of each injection and a subsequent 3×3 median filter were applied for noise reduction; third, a fixed threshold of between 4.7% and 9.1% of the maximum spray intensity was defined for each cycle and the images were then binarized.

Geometric parameters were extracted from the binarized spray images to compare the spray morphology, contrasting the numerical and experimental results. The maximum axial penetration, termed L in Figure 3, was defined as the maximum distance from the binarized liquid spray boundary to the injector tip along the injector axis. A 0.95 percentile criterion was used to define L (based on the projected spray area onto the injector axis; not represented in Figure 3) in order to mitigate the influence of outliers. Similarly to the method outlined by Payri et al.,[40] the global spray angle α was defined as the angle between two linear least-square fits along the outer spray contours between 1% and 50% of L.

Since exactly the same setup for Mie scattering as used by Geschwindner et al.[18] was applied in this work, additional details regarding the optical resolution, field of view, spray binarization, parameter extraction, etc. can be found in the *Mie scatter imaging* section of Geschwindner et al.[18]

High-speed PIV. Using the same spray and motor operating conditions as with Mie scattering, 143 consecutive

cycles of high-speed PIV data were acquired in the symmetry plane at a $1°$ crank angle resolution from $290°$ beforeTDC until TDC. A standard PIV setup was employed consisting of two laser sheets from frequency-doubled Nd:YAG cavities with crank-angle-optimized time separation dt. In the same manner as with the Mie scattering light source, the laser sheets (thickness: 1 mm at 13.5% of the maximum intensity) entered the cylinder via the piston and illuminated an approximate field of view of 60×55 mm^2. A high-speed Phantom v1610 CMOS camera equipped with a Sigma lens (105 mm F2.8 Macro, $f/11$) and a 532 nm band-pass filter acquired double-frame images of laser-illuminated silicone particles (Dow Corning DOWSIL 510 Fluid, 0.5μm) that were introduced with the air far upstream of the intake valves to ensure homogeneity.

The post-processing of image pairs was conducted in the commercial software DaVis 8.4.0 (LaVision GmbH). The first step used in calculating the vector fields was sliding background subtraction at a scale of 4 pixels to help reduce the effects of reflections causing high-intensity fluctuations. Next, a geometric mask was used to remove engine features which cause reflections, and an algorithmic mask was used to remove moving bodies such as the piston, valves, and liquid spray, which induce unwanted saturation due to multi-scattering. To calculate the vectors, a multi-pass cross-correlation of decreasing window size was used (first two passes: 64×64 pixels, square weighting function, 50% overlap; next two passes: 32×32 pixels, adaptive PIV Gaussian weighting function, 75% overlap). After each cross-correlation pass, post-processing (peak ratio criterion: $Q < 2$; universal outlier detection: 5×5 pixels region) was carried out to help improve the estimation of the next pass. Finally, after the final cross-correlation pass, another peak ratio criterion was applied ($Q < 1.3$), a universal outlier detection median filter of the same size as in multi-pass processing was used, and a group vector removal criterion of five vectors was applied to remove any spurious vectors missed by the median filter. To interpret the flow fields, the presented results are phase-averaged, which involves the vector field for each crank angle over all cycles being averaged, with a minimum number of 25 vectors required at each interrogation window for the average to be calculated. For more details on the PIV setup, data acquisition and post-processing, see Geschwindner et al.[18]

Numerical simulation setup

Calculations were performed with the open-source OpenFOAM® CFD software under a RANS approach with the standard $k - \varepsilon$ model employed for turbulence modeling. The Pope[41] correction was applied to the transport equation of the turbulence dissipation rate ε by increasing the $C_{1\varepsilon}$ parameter to a value of 1.55. This enabled a better prediction of both the spray

Table 3. Details of the CVC operating condition.

Condition	G3[42]
Fuel	Iso-octane
Fuel pressure	20 MPa
Fuel temperature	363 K
Fuel mass	10 mg
Bulk gas	N_2
Bulk gas temperature	333 K
Bulk gas density	1.01 kg m^{-3}

morphology[30,43] and air entrainment during and after the injection process.[44]

Iso-octane was adopted as the fuel with liquid thermophysical properties calculated as a function of the temperature according to the formulations provided by the National Institute of Standards and Technology (NIST).[45] The gas phase was modeled as a perfect mixture of ideal gases with the heat capacity described by NASA polynomials.[46]

Every simulation was carried out using the Pressure-Implicit with Splitting of Operators (PISO) algorithm[47] without fields under-relaxation. The convective terms were discretized by a second-order Gauss Limited Linear scheme with the exception of the velocity convection for which a Gauss Linear Upwind scheme was employed. The diffusive terms were managed with a Gauss cell-limited scheme while the first-order explicit Euler approach was adopted for time discretization. The simulation time-step was kept fixed and equal to 1μs for each calculation.

Constant-volume chamber configuration

The numerical spray setup which was employed for the full-cycle engine simulation was first investigated and tested in the constant-volume chamber. Consistently with the engine case, the ECN Spray G3 operating point was chosen as a benchmark for evaluating the accuracy of the unified numerical model and to study the spray evolution during a typical early injection event in DISI engines. The main characteristics of the vessel simulation are summarized in Table 3.

The CVC computational grid consists of a structured 3D domain of hexahedral cells with a constant size of 0.5 mm. To ensure that the grid was consistent with the engine simulation, Adaptive Mesh Refinement (AMR) was not employed. It was also shown that it could potentially have a negative effect on the entrainment when applied to multi-hole GDI spray modeling.[32]

The CVC numerical results were assessed in terms of axial liquid and vapor penetrations, in-plume liquid distribution, and overall spray morphology against dedicated experimental data presented by the University of Melbourne at the ECN6 Workshop.[18] Within this context, the axial vapor penetration was experimentally measured by means of a Schlieren technique and computed as the maximum axial distance from the injector

tip, where a mixture fraction of 0.1% is found. The calculated axial liquid penetration was investigated by examining two different thresholds of a specific projected liquid volume (PLV) field, defined employing a methodology that was first introduced at the ECN6 Workshop.[49] Experimentally, the parameter was provided by the University of Melbourne based on their Diffuse Back-Illumination (DBI) measurements.[48]

This method replaced the computation of the axial liquid penetration by means of the liquid mass, an approach which is characterized by low accuracy when applied after the end of injection. In this context, the PLV was defined using Equation 14

$$\int_{-y_\infty}^{y_\infty} LVF dy \tag{14}$$

where LVF is the local Eulerian liquid volume fraction (expressed in mm_{liquid}^3/mm^2) and y represents the cross-stream direction. Under the assumption of a monodisperse droplet size distribution, the liquid optical thickness τ along the beam path was experimentally coupled to the extinction by means of equation (15):

$$\tau \frac{\pi \frac{d^3}{6}}{C_{ext}^*} = \int_{-y_\infty}^{y_\infty} LVF dy \tag{15}$$

The term d represents the droplet diameter (equal to $7\,\mu m$ according to Sauter Mean Diameter (SMD) measurements performed by General Motors) and C_{ext}^* is the extinction cross-section derived from Mie theory (equal to $44.6 \cdot 10^{-6}\,mm^2$ for Spray G with iso-octane). The SMD in each control volume is defined using equation (16)

$$d_{3,2} = \frac{\sum_i n_i d_i^3}{\sum_i n_i d_i^2} \tag{16}$$

where n_i is the number of spray particles in the control volume and d_i is the corresponding diameter. The C_{ext}^* constant, depending on the droplet size, wavelength, and collection angle, was assumed to be equal to 225 mrad at 633 nm. The two adopted thresholds for defining the axial liquid penetration are $2 \cdot 10^{-3}\,mm_{liquid}^3/mm^2$ ("high" threshold) and $0.2 \cdot 10^{-3}\,mm_{liquid}^3/mm^2$ ("low" threshold), as reported in the ECN6 Guidelines.[49] The axial liquid penetration was computed as the maximum axial position of any plume with a projected liquid volume lower than the selected threshold.

Further, the projected liquid volume field allowed for a morphological comparison between experimental and computed sprays by means of PLV maps which are generated from simulation data employing the methodology described in Figure 5. In more detail, the Eulerian LVF field is derived from the Lagrangian liquid, integrated along different lines, and then projected onto a 2D background mesh to derive the projected liquid volume maps of the spray.
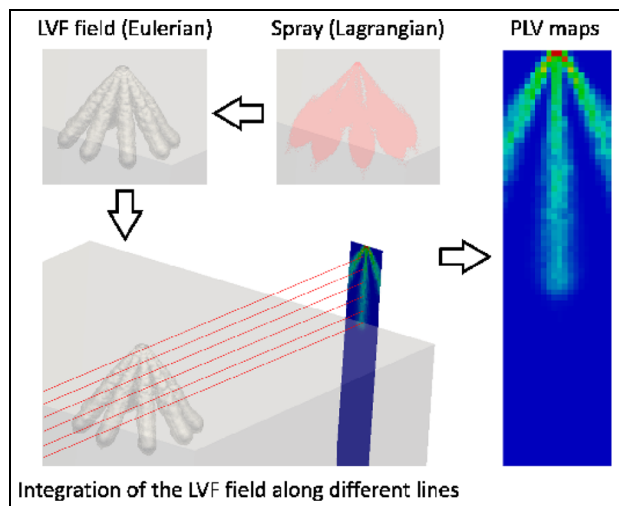

Figure 5. Numerical definition of the PLV maps.[23,48]

Engine configuration

For the engine simulations, a key-grid approach was adopted.[50] With this methodology, a computational grid is generated at the initial crank angle, then the mesh is deformed by solving a cell-motion Laplace equation[51,52] applying the prescribed piston and valve motion. When the maximum non-orthogonality of the grid falls above 75°, a new mesh is generated. The process is iterated until the entire cycle is covered. This approach has been used and validated in previous works.[20,50,53,54]

The computational domain consists of a structured hexa-dominant grid, oriented along the cylinder, with a maximum cell size of 2 mm, an example of which is shown in Figure 6(b). The castellated algorithm incorporated in the *snappyHexMesh* software was employed to generate the grids. Cells on the intake valve walls were refined up to 0.5 mm, to better predict the flow detachment from the valve stems. The cells in the cylinder region were further refined up to a maximum size of 1 mm, except during the injection phase, when they were refined up to a maximum size of 0.5 mm to better capture the large gradients occurring in the spray jets.

The minimum valve lift in simulation is equal to 0.5 mm. The valve timing used in the simulation is shown in Table 4. It is measured with a valve lift of 0.25 mm (half of the minimum valve lift in simulations). This slightly enlarges the opening time of the valves during the simulation, resulting in the inclusion of the mass and momentum exchanged while the valve lift is below the minimum value.[55]

Phase-averaged experimental pressures were applied as boundary conditions in the intake and exhaust manifold, as seen in Figure 6. These boundary conditions allow the dynamic effects to be taken into account in the ducts. This must be considered in this type of engine configuration for an accurate simulation.[56] Scalable wall functions were used for the treatment of the velocity boundary layer. Averaged temperatures of
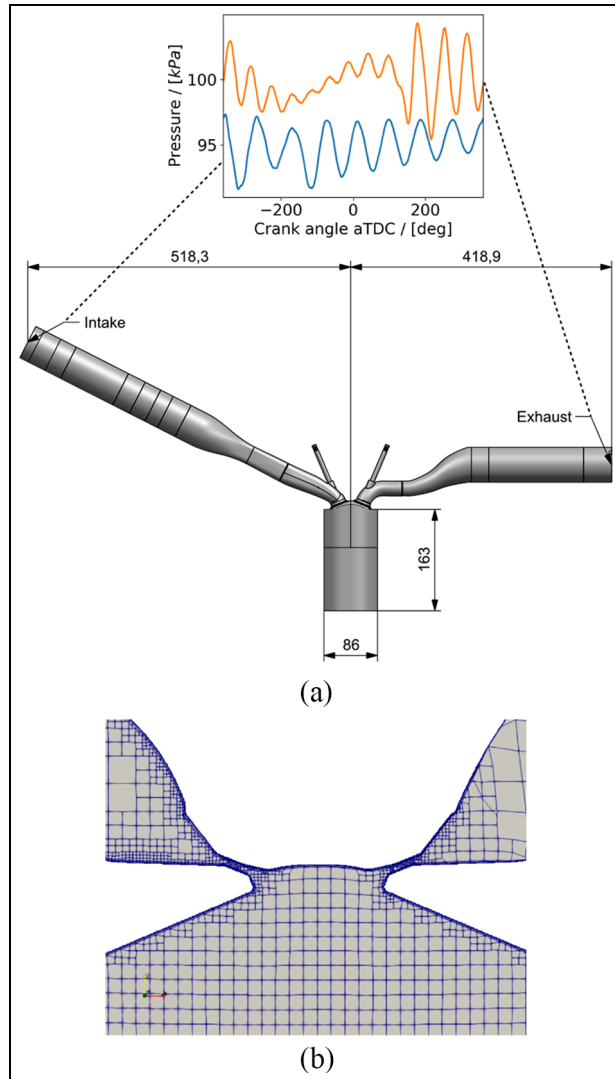
(a)

(b)

Figure 6. (a) Shows the pressure imposed at intake and exhaust port, equivalent to the experimental phase average. The oscillation are caused by the manifold fluid dynamics and (b) shows a detail of the hex-dominant mesh on the valve plane (z = 19 mm) during the overlap phase. Both intake and exhaust valve gap are visible.

Table 4. Valve timing adopted at the valve lift of 0.25 mm.

Valve	Opening	Closing
Exhaust	127° afterTDC	351° beforeTDC
Intake	347° afterTDC	132° beforeTDC

308 K from the experiment were imposed on the intake and exhaust manifolds. On the cylinder walls, the temperature of the engine coolant fluid was imposed at 60°C(≡333.15 K). The entire setup was validated in a previous work in a motored condition with and without the spray.[20] To initialize the in-cylinder conditions before the injection, a cycle was simulated from the beginning of the exhaust phase until the start of the injection. The electric start of injection was imposed
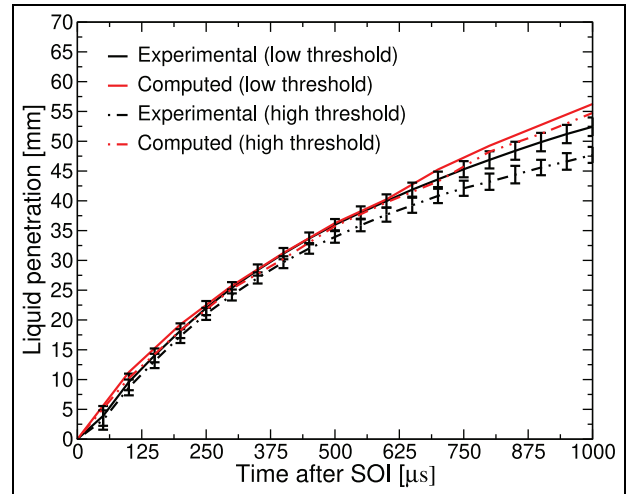
Figure 7. Spray G3 condition: comparison between computed and experimental[48] axial liquid penetrations for both thresholds.[32] SOI equal to simulation start-time, EOI equal to 0.78 ms.

equal to 270° beforeTDC with a hydraulic delay equal to 307 μs, in accordance with experimental measurements.[29] All the other properties of the spray have been reported in the "Constant-Volume Chamber Configuration" and "Experimental Setup" sections.

For comparison with experimental measurements, the axial penetration and spray angle were not calculated on a mass basis; instead, a numerical Mie scattering signal was calculated. At each parcel, a Mie signal is assigned on the basis of equation (17):

$$S = n_p \frac{\pi}{4} d_p^2 = \frac{m_p}{V_p} \frac{\pi}{4} d_p^2 \tag{17}$$

where n_p is the number of particles defining a parcel (i.e. the mass of the parcel m_p divided by the volume of the particle V_p) and d_p is the diameter of the particle, with the assumption that the Mie scattering signal is proportional to the projected area of the particles and the spray particles are spherical.

Afterwards, a 2D histogram of the numerical signal was computed on the same line of sight as the experiments (frontal view), with the bin size equal to the resolution of the experimental measurement. The signal was normalized based on the maximum value extracted from the entire injection. As a final step, the same post-processing procedures were adopted as described in the "Experimental Setup" section.

Results: Spray in constant-volume chamber

In this section, the results from the Spray G3 CVC simulation are discussed and compared against experimental data available from latest ECN Workshops.

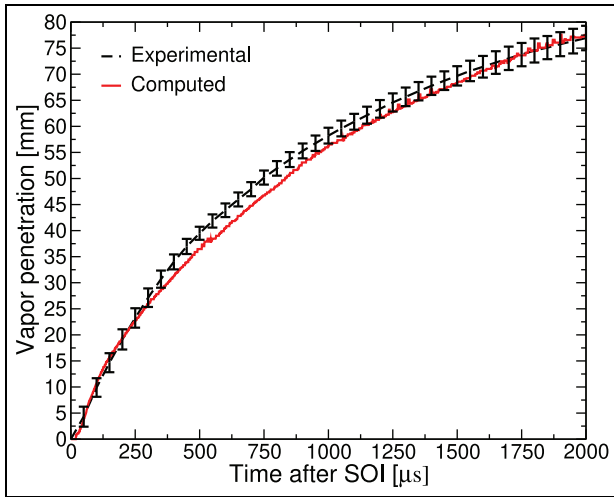Figure 7 reports the comparison between experimental and computed axial liquid penetration profiles.

Figure 8. Spray G3 condition: comparison between computed and experimental[48] axial vapor penetrations.[32] SOI equal to simulation start-time, EOI equal to 0.78 ms.

Good accuracy is achieved by the calculations albeit with a slight overestimation which is observable after the end of injection. Figure 8 further assesses the consistency of the adopted numerical spray model by showing a well captured computed axial vapor profile up to the simulation end-time.

Figure 9(a) to (c) show the PLV-based axial evolution of the in-plume liquid distribution at early (0.3 ms), late (0.6 ms), and post-injection (0.9 ms) times. Globally, the computed profiles show a good agreement with the experimental trends. In greater detail, a small overestimation in the simulations can be observed at axial distances greater than 20 mm. This is to be expected because the far-field parcels are subjected to low-intensity breakup and evaporation phenomena as the G3 operating point is characterized by ambient conditions typical of an early-injection event.

Closer to the injector nozzle, an analysis based on the axial PLV profiles is not a feasible means of assessing the accuracy of the model, in part because of experimental data loss below a 5 mm axial distance. Nevertheless, it can be stated that adequate interaction between atomization and secondary breakup is achieved since both the axial liquid and vapor penetration profiles are computed with a good level of accuracy by the proposed model. The interaction between these quantities is in fact particularly complex to reproduce near the injector nozzle in the case of low-evaporating sprays. An overall improvement in
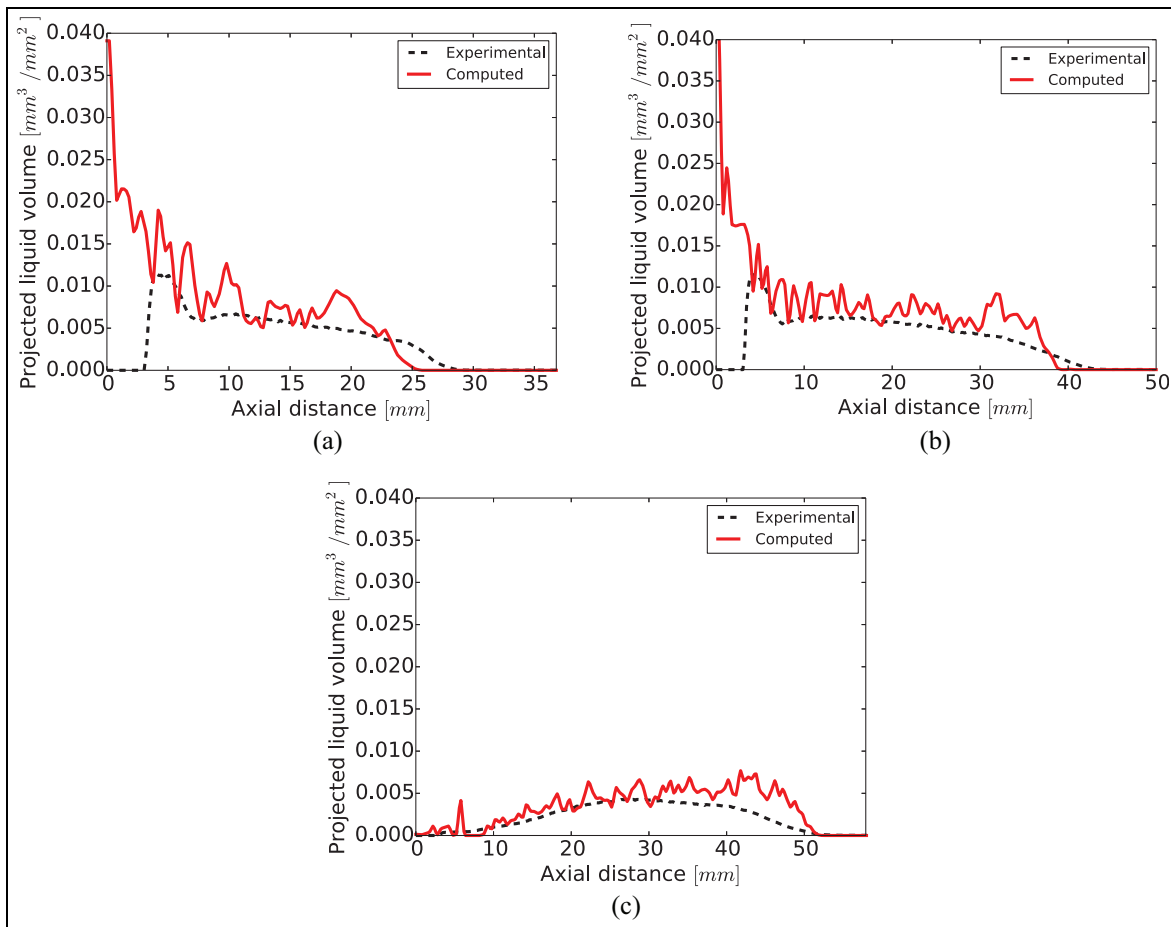
Figure 9. Spray G3 condition, axial PLV profiles: comparison between experimental[48] results and computed data: (a) 0.3 ms after SOI, (b) 0.6 ms after SOI, and (c) 0.9 ms after SOI.
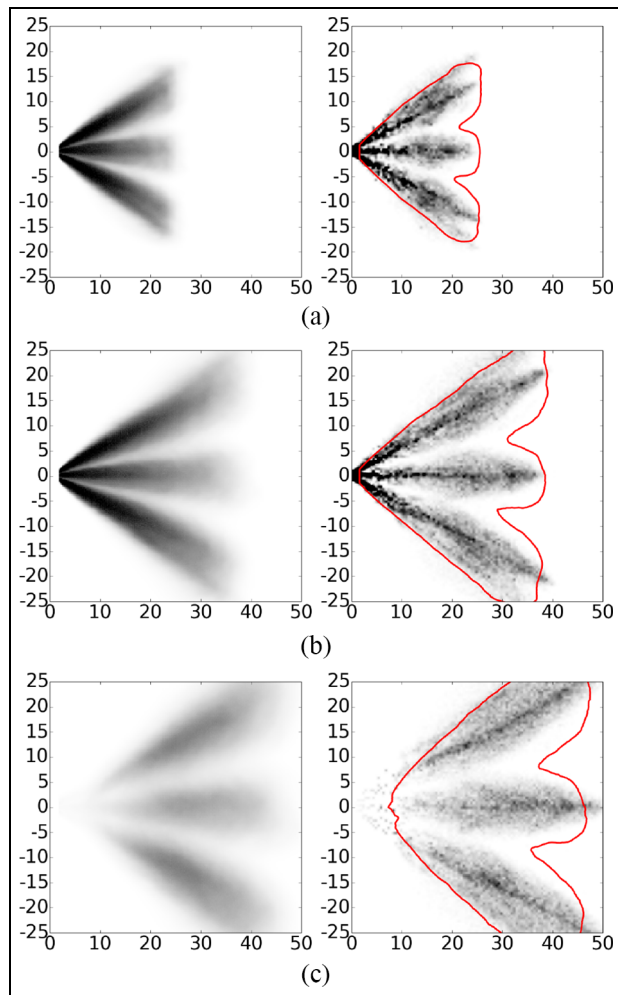
Figure 10. Spray G3 condition: comparison between PLV maps for experiments[48] (left) and computed spray (right). Numerical PLV maps enveloped in extracted experimental spray outline contour (LVF threshold of $0.001\,\mathrm{mm}^3/\mathrm{mm}^2$). Global LVF range is $0 - 0.01\,\mathrm{mm}^3/\mathrm{mm}^2$. Axes dimensions are reported in mm: (a) $0.3\,\mathrm{ms}$, (b) $0.6\,\mathrm{ms}$, and (c) $0.9\,\mathrm{ms}$.

Figure 11. Computed SMD for CVC G3 case (red dot) validated against literature-based thresholds for multi-hole sprays.[57]
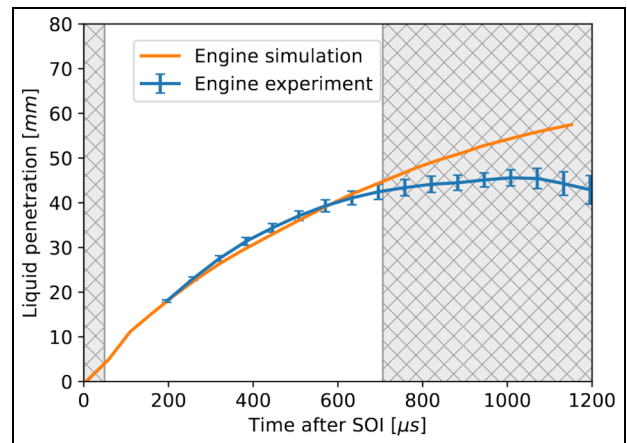
Figure 12. Liquid penetration of Spray G comparing the experimental engine data and engine simulation.

accuracy is observed compared to the results achieved in previous simulations carried out with a more conventional spray setup.[23]

A PLV-based, morphological spray comparison between the experiments (left) and simulations (right) is reported in Figure 10(a) to (c) for times after SOI respectively equal to $0.3\,\mathrm{ms}$, $0.6\,\mathrm{ms}$, and $0.9\,\mathrm{ms}$. An outline contour of the spray was extracted from available experimental data with a liquid volume fraction threshold of $0.001\,\mathrm{mm}^3/\mathrm{mm}^2$ and it was superimposed on the computed PLV maps. The results show that good agreement is achieved between the spray plume shapes for each reported time in both radial and axial direction.

Finally, the average computed Sauter Mean Diameter (SMD) is shown in Figure 11 for the CVC G3 operating condition. The value falls within specific low and high experimental thresholds derived by Hammer et al.[57] for multi-hole sprays as a function of the injection pressure.

Results: Spray in engine

Spray morphology

This section discusses the results of the experiment and the simulation of the ECN Spray G mounted in the Darmstadt engine. First, the penetration, angle and morphology of the spray are compared against the experiment. Then, gas velocities on the tumble plane are compared against the experiment, both before and after injection. Finally, the air-fuel mixture evolution is analyzed alongside the gas velocity field on four different planes. These data, available only from the simulation, show the two-way interaction between the three-dimensional flow and the spray.

Figure 12 presents a comparison of the liquid penetration in the experiment and numerical simulation. The comparison is limited to the time between $49\,\mu s$ and $706\,\mu s$, which corresponds to the time interval of 5% and 95% of the injected momentum. The
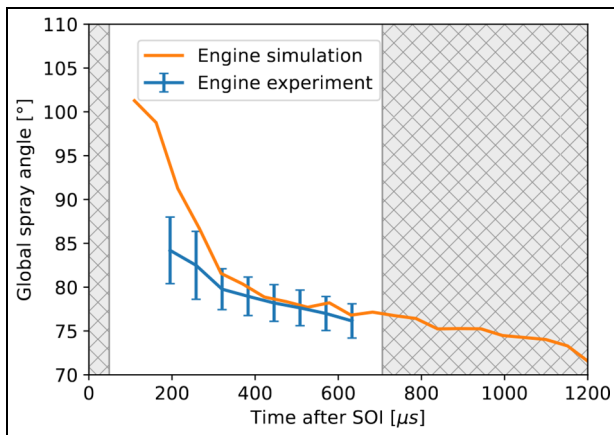
Figure 13. Global angle of Spray G3 comparing the experimental engine data and engine simulation.

Figure 14. Asymmetry of the spray angle for the experimental engine data and engine simulation.

experiment and numerical simulations are shown to match throughout the duration of the injection. The breakup model is able to predict the spray penetration, not only into a static environment but also with in-cylinder flow.

It is noteworthy that the results are obtained without any further parameter adjustment. However, it can be observed that the penetration is over-predicted after the end of the injection, along with the spray evaporation. The reduction in the liquid mass and the challenging engine configuration increase the difficulty to analyze the spray morphology.

In Figure 13, the global spray angles are compared. Firstly, it is clearly visible that the spray angle decreases during the injection both in the experimental and the simulated engine. With the exception of the early stage of the injection, where an over-prediction of the numerical simulation is observed and the experimental results have a high degree of uncertainty as the view of the spray is obstructed by the intake valve, the computed spray angle matches the experiments well. This confirms that the breakup model is able to predict the spray evolution during the injection.

In Figure 14, the asymmetry factor F_a for the spray is, contrasting the experimental engine and the engine simulation. The asymmetry of the spray in the engine is clearly visible, with the spray opening on the exhaust side (labeled *overflow* in Figure 3). The trend is predicted well by the numerical model and can be explained by the presence of an intake flow which drags and deforms the plumes. The effect of the intake flow on the plume is investigated in more detail in the "Spray-Flow Interaction" and "Inter-Plume Interaction" sections.

Figure 15 shows the evolution of the spray morphology, comparing experimental Mie scattering signals of the engine spray (average of binarized sprays) to the corresponding numerical results. For each spray snapshot, the two closest times are compared. Figure 15(a) shows the early phase of the injection. The spray is seen
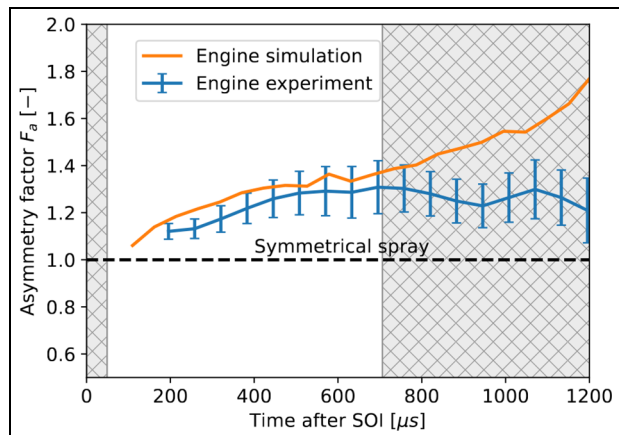
to impinge on the spark plug from the very beginning of the injection. During the injection (Figure 15(b) and (c)), the computed spray is extremely similar to the experiment. The plumes are still distinct and there are no visible signs of the spray collapsing. Therefore, the breakup phenomena play a relevant role in the evolution of the spray morphology, and the model implemented describes this accurately.

In addition, both the experiment and simulation show wetting of the spark plug (Figure 15(b) and (c)). The impingement of the *overflow* plume on the spark plug (see Figure 3 for the definition of *overflow* plume) contributes to the positive asymmetry factor visible in Figure 14.

In Figure 15(d), the EOI spray morphology is reported. At this late injection phase, differences can be observed between the simulations and experiments, especially at the tip of the spray. This is strictly related to the penetration over-prediction shown in Figure 12 and discussed previously.

Figure 16 shows the gas velocity along the injector axis *during* the injection. The sign of the gas velocity is set according to the local coordinate system illustrated in Figure 3. For comparison, the velocity from the CVC simulation is also shown.

In the CVC, the spray induces a negative axial gas velocity (i.e. oriented toward the injector tip). In the engine, the intake flow generates velocities directed axially outwards from the injector ($V_y^* > 0$). However, like the CVC, the spray tends to counteract the intake flow but not sufficiently to induce negative axial velocity.

The interaction of the spray with the in-cylinder intake flows will be investigated further in the following sections.

Spray-flow interaction

In Figures 17 and 18, the velocities of the gas phase in the tumble plane are compared on vertical and horizontal profiles, respectively. The blue lines identify the gas
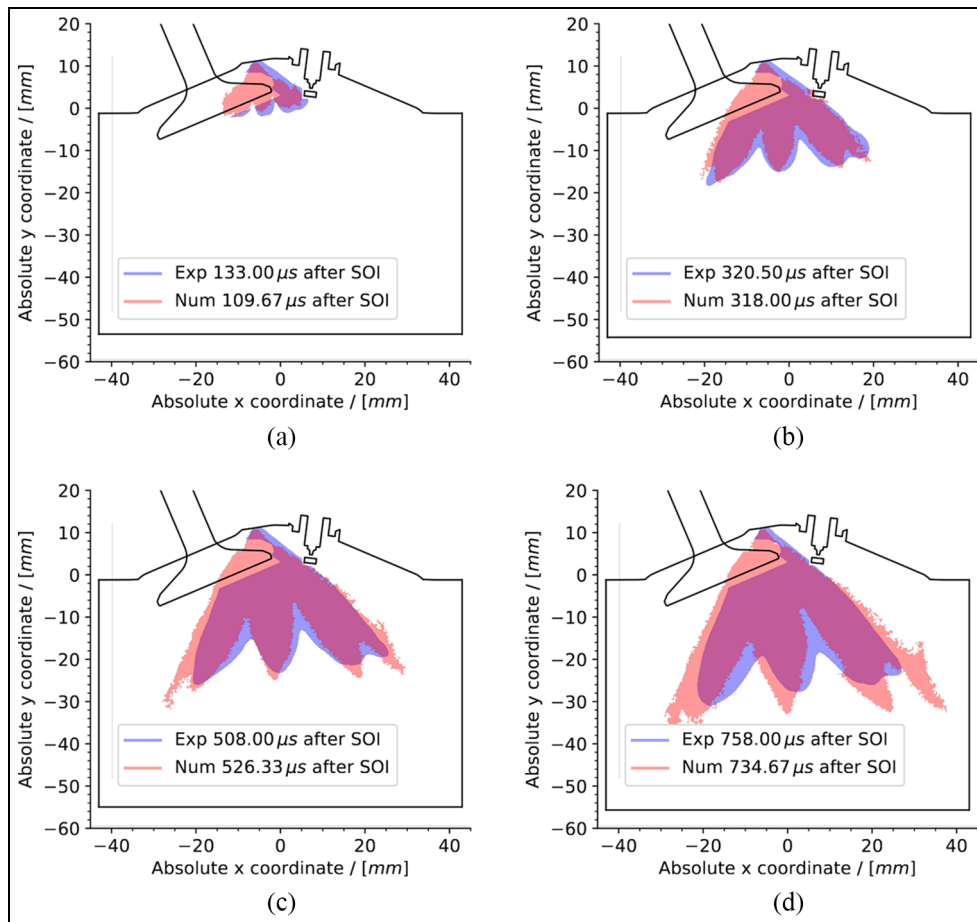
Figure 15. Comparison of the binarized Mie scattering spray signals, contrasting experimental and numerical results. The same filtering and post-processing algorithms are applied to both signals. The red shapes represent the numerical spray, while light-blue shapes represent the experimental spray. The results are compared by choosing the two closest available time snapshots. Engine features are indicated by black lines: (a) early injection, (b) mid-early injection, (c) mid-late injection, and (d) end injection.
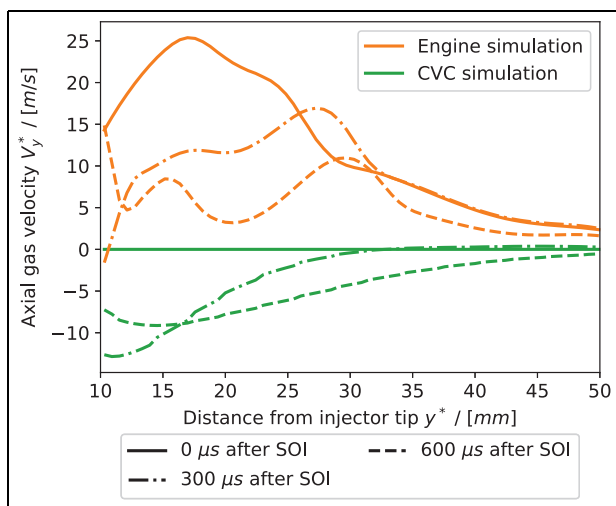
Figure 16. Axial gas velocity during the injection of the computed spray in the CVC and engine. The velocities are sampled along the line $x^* = 0$ (i.e. along the injector axis). The coordinate system relative to the injector is used.

velocities before injection ($0°$afterESOI), while the red lines identify the gas velocity when the fuel is almost fully evaporated ($10°$afterESOI). Good agreement is seen before the injection, validating the numerical setup of the motored engine. The gas velocity is clearly directed toward the exhaust valve and downward, playing a relevant role in spray asymmetry.

After the injection, the velocity trend matches reasonably well, and it is seen that the global morphology of the in-cylinder flow does not change drastically after the injection, indicating that the intake flow tends to recover its morphology *after* the injection. This confirms that the effects of the spray are convected away by the intake flow. The comparison is reasonable considering the numerical challenge of the configuration, the increased uncertainty of the PIV measurements shortly after injection, and the absence of any parameter adjustment.

To gain further insights we study the spray evolution using nondimensional parameters, because is possible to compare this case with other sprays in a crossflow channel. The study by Welss et al.[58] investigated different GDI injector types and proposed some nondimensional parameters to describe the transversal spray deviation. In that work, the spray penetration is
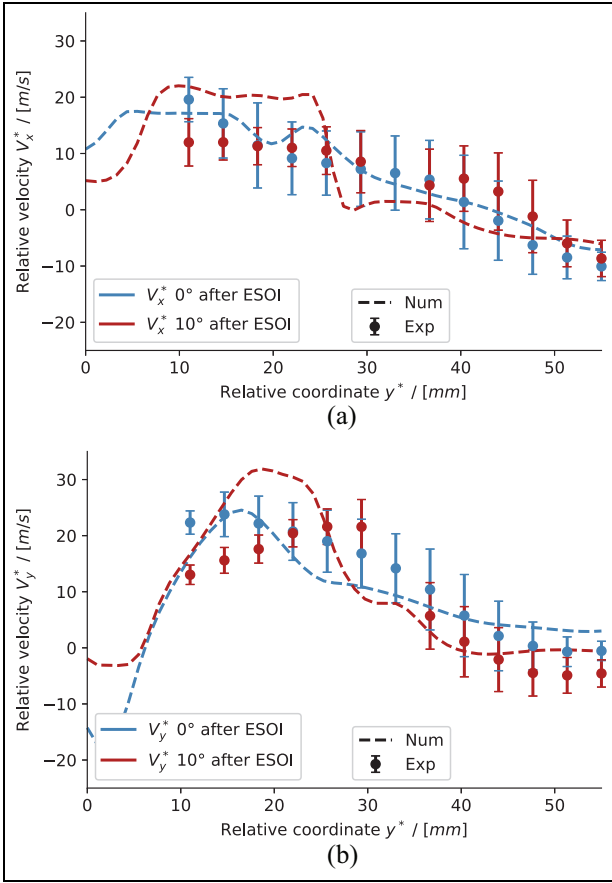
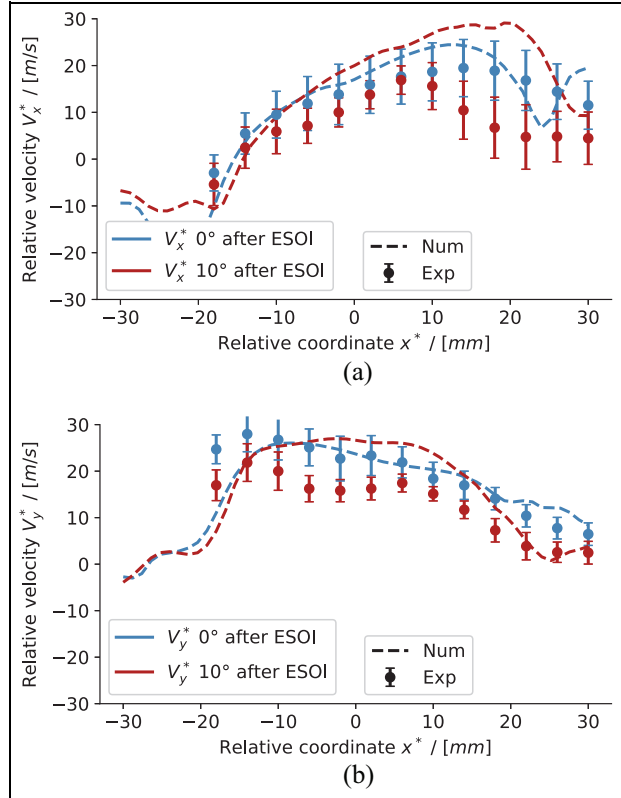**Figure 17.** Comparison of gas velocity along the line $x^* = 0$ mm (i.e. along the injector axis). Velocities before and after injection are displayed. The coordinate system is relative to the injector. On the top row, the velocity component V_x^* are compared. On the bottom row, the velocity components V_y^* (i.e. along the injector axis) are compared. The error bar represents the standard deviation of the measured velocities: (a) velocities V_x^* and (b) velocities V_y^*.

Figure 18. Comparison of gas velocity along the line $y^* = 15$ mm (i.e. perpendicular to the injector axis). Velocities before and after injection are displayed. The coordinate system is relative to the injector. On the top row, the velocity components V_x^* are compared. On the bottom row, the velocity components V_y^* are compared. The error bar represents the standard deviation of the measured velocities: (a) velocities V_x^* and (b) velocities V_y^*.

nondimensionalized dividing it by 70 mm (the size of the cross-flow channel), while the radial deviation of the center of the spray from the centerline is nondimensionalized, dividing it by 50 mm.

While is not possible to extract the center of the spray with the same procedure described by Welss et al.,[58] a similar procedure is applied to the numerical results discussed in this work. Based on a consideration of the geometry, the nondimensional deviation K_s is evaluated as:

$$K_s = \frac{0.5 * L \sin(\alpha_r - \alpha_l)}{50 \text{ mm}} \quad (18)$$

The nondimensional penetration is evaluated as:

$$L_s = \frac{L}{70 \text{ mm}} \quad (19)$$

To estimate the crossflow velocity $V_{x,s}^*$ the radial velocity V_x^* has been averaged along the injector axis and during the injection. The velocity $V_{x,s}^* = 11.4$ m/s has been obtained.

Figure 19 shows the nondimensional deviation of the spray during the injection. The color of the line identifies the nondimensional penetration. It can be observed that the deviation increases with the penetration. At nondimensional penetration of $L_s = 0.3$ the nondimensional deviation $K_s = 0.03$ has been found, while at a nondimensional penetration of $L_s = 0.6$ the nondimensional deviation increases to $K_s = 0.08$. These values are comparable with the values obtained for the symmetric multi-hole injectors under similar crossflow velocity presented by Welss et al.[58] This confirms the important effect that the in-cylinder flow has on the asymmetry of the spray.

Despite the short spray duration, the momentum injected is relevant, so it is interesting to observe the interaction between the flow and the spray *during* the injection. Figure 20 depicts the evolution of the velocity and the iso-octane vapor mass fraction in the tumble plane.

Before the injection (Figure 20(a)), the tumble intake port induces a partial vortex (labeled "A"). Without the injection, the flow field does not change significantly from the flow displayed in Figure 20(a) during the time interval in which the injection would occur
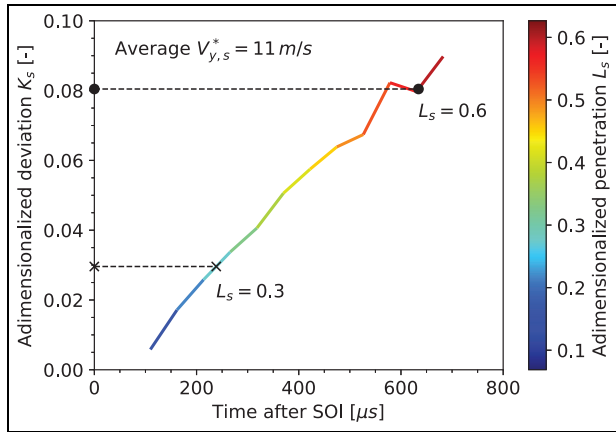
Figure 19. Nondimensional deviation K_s of the spray during the injection. The line coloring identifies the adimensional penetration L_s. Average crossflow velocity $V_{x,s}^*$ is annotated.

(see Figure 21). This makes it possible to observe the flow structures generated by the spray injection.

At the beginning of the injection (Figure 20(b)), the intake flow visible on the tumble plane is seen to be strong enough to prevent the formation of vortices on the tips of the plumes. Vortice formation was not observed with late injection on the same spray and engine.[18] In that operating condition, the in-cylinder flows point upwards and are about 2.5 times weaker.[18] As discussed above, air flowing from the intake side to the exhaust side tends to make the spray asymmetrical. The interaction with the spark plug (labeled "S") is also visible.

In Figure 20(c), the injector introduces the maximum amount of momentum during the injection event. The tip of the overflow plume interacts with the partially formed vortex ("A"), developing a full vortex. This vortex induces a flow directed upward and to the right (red arrow marked "1"). This flow has two effects: first, it counteracts the downward axial flow, stabilizing the outer spray angle, and second, it pushes the spray toward the exhaust, increasing the spray asymmetry.

In Figure 20(d), after the end of injection, the vortex is thus fully developed. The flow labeled "1" reaches the maximum development. It is also clearly visible that the airflow coming from the intake side of the spray further dilutes the left plume, reduces the global angle α, and increases asymmetry (red arrow marked "2").

The results clearly demonstrate that the spray interacts strongly with the intake flow, generating a vortex which stabilizes the spray and increases the spray asymmetry itself (the latter has also been observed in experimental measurements, see Figure 14).

Figure 22 shows the flow at $10°$ afterESOI ($1780\,\mu s$ after SOI). It can be stated that the intensity of the upward flow induced by spray recirculation lessens (red label "1"), and the flow tends to return to the state before the injection (shown in Figure 20(a)). This is in accordance with the comparison of velocities shown in Figures 17 and 18.
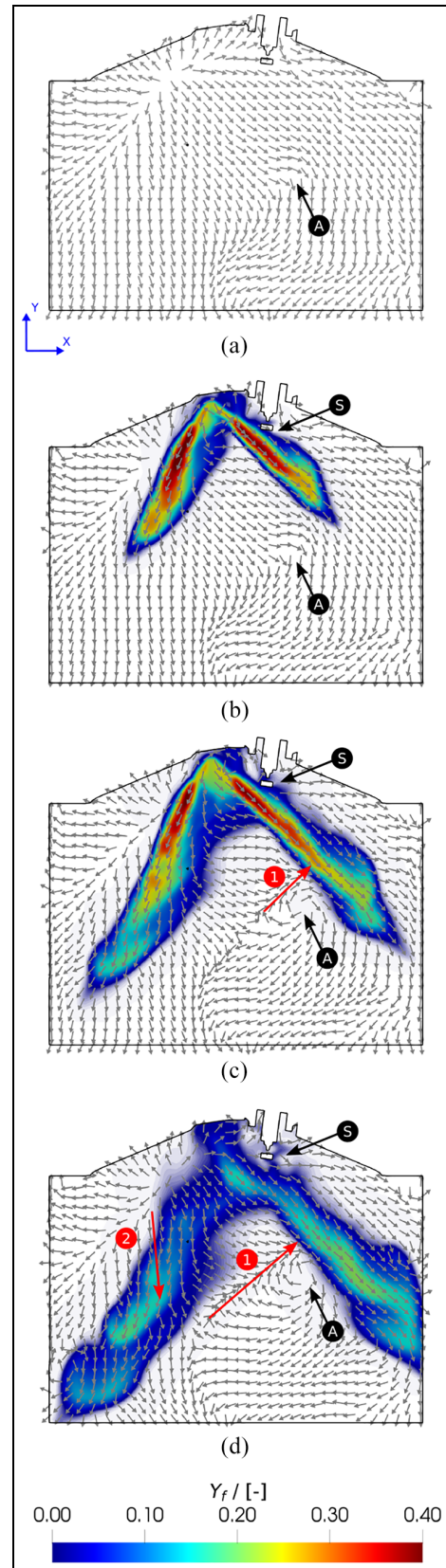

Figure 20. Velocity field and iso-octane vapor mass fraction in the tumble plane during the injection of the engine simulation. The ESOI is set up at $270°$ beforeTDC: (a) $1.25°$ after ESOI $\approx -46.6\,\mu s$ after SOI, valve lift = 9.22 mm, (b) $3.25°$ after ESOI $\approx 370.1\,\mu s$ after SOI, valve lift = 9.27 mm, (c) $5.0°$ after ESOI $\approx 734.7\,\mu s$ after SOI, valve lift = 9.31 mm, and (d) $6.75°$ after ESOI $\approx 1099.2\,\mu s$ after SOI, valve lift = 9.35 mm.
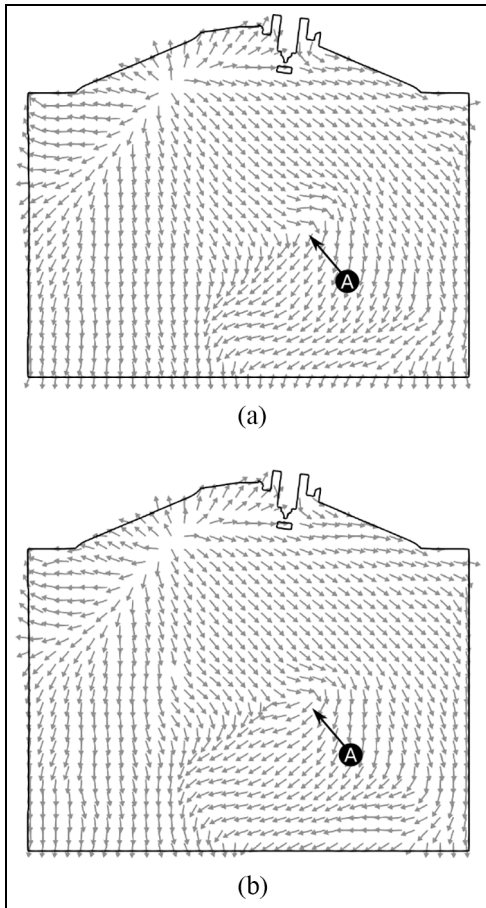
Figure 21. Velocity field in the tumble plane of motored case without any injection. It can be observed that the main structures of the fluid are similar to those present before injection: (a) 5° after ESOI and (b) 10° after ESOI.
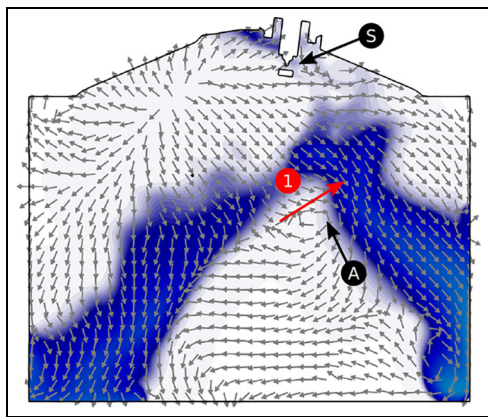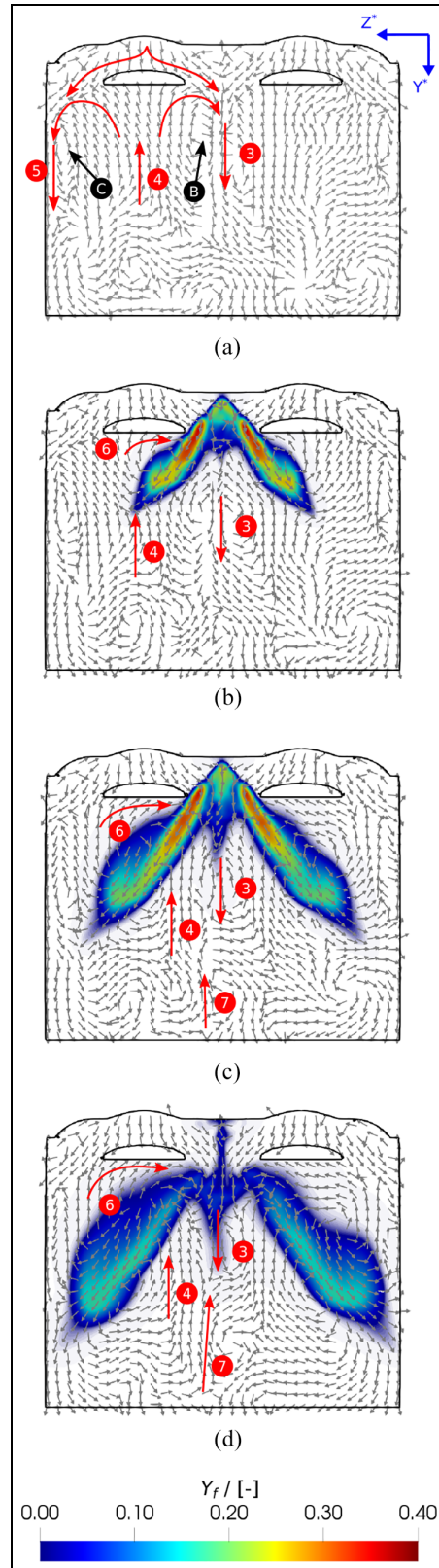

Figure 22. Velocity fields and iso-octane vapor mass fraction in the tumble plane 10° afterESOI of the engine simulation. Compared to the flow field before the injection (s. Figure 20(a)). It can be seen that the flow has not changed its morphology.

Spray-valve interaction

In this section, the interaction between the plumes and the intake valves is investigated. The plumes leaving the tumble plane (normal to the *z* axis) are affected the most by the intake valves.

Figure 23. Velocity fields and iso-octane vapor mass fraction in the frontal plane during the injection of the engine simulation. Only flow structures on the left are highlighted. The ESOI is set up at 270° beforeTDC: (a) 1.25° after ESOI ≈ −46.6 μs after SOI, valve lift = 9.22 mm, (b) 3.25° after ESOI ≈ 370.1 μs after SOI, valve lift = 9.27 mm, (c) 5.0° after ESOI ≈ 734.7 μs after SOI, valve lift = 9.31 mm, and (d) 6.75° after ESOI ≈ 1099.2 μs after SOI, valve lift = 9.35 mm.
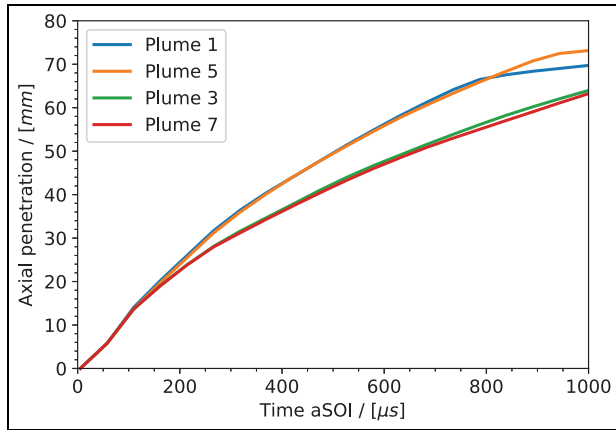
Figure 24. Plume penetration in simulated engine. For each plume, penetration is defined as the distance along the injector hole which contains 99% of the plume mass. Plume labels as in Figure 3.

To investigate the evolution of these plumes and their interaction with the intake valves, the domain is sliced on the frontal plane (see Figure 4), and the resulting flow and the vapor fuel fractions are displayed in Figure 23.

In Figure 23(a), the velocity field before the injection is visible. Due to the intake flow, the velocity field is characterized by two downward flow structures, one located on the tumble plane (labeled "3") and one by the liner (labeled "5"), and an upward flow directed toward the valve plates (labeled "4"). As a consequence, two vortices form under each intake valve plate (labeled "B" and "C").

During the injection, as seen in Figure 23(b) and (c), a recirculation flow (labeled "6") forms on the outer sides of the plumes, shielded from the strong intake flow by the valves. It can also be seen in Figure 23(c) and (d) that the upward flow (labeled "4") directed toward the valve plates increases the dilution and stabilizes the spray itself, despite the downward flow in the tumble plane (labeled "3"). These two effects lead to a strong radial flow and higher dilution compared to the plumes laying on the tumble plane.

To confirm the reduced penetration of the plumes outside the tumble plane, the plot of individual plume penetration is shown in Figure 24. It can clearly be noted that plume 1 (on the tumble plane – overflow) and plume 5 (on the tumble plane – underflow) penetrate more than plumes 3 and 7 (on the frontal plane).

The induced tumble flow described in the section on "Spray-Flow Interaction" is indicated with the red arrow marked "7" in Figure 23(c) and (d) and it counteracts the downward motion. The interaction between these two flow structures energizes the two upward flows ("4") beneath the intake valve plate, further increasing the dilution and the spray stabilization.

As a secondary phenomenon, the large amount of air flowing at the tip of the injector strongly dilutes the top of the spray, with the formation of a coherent vapor
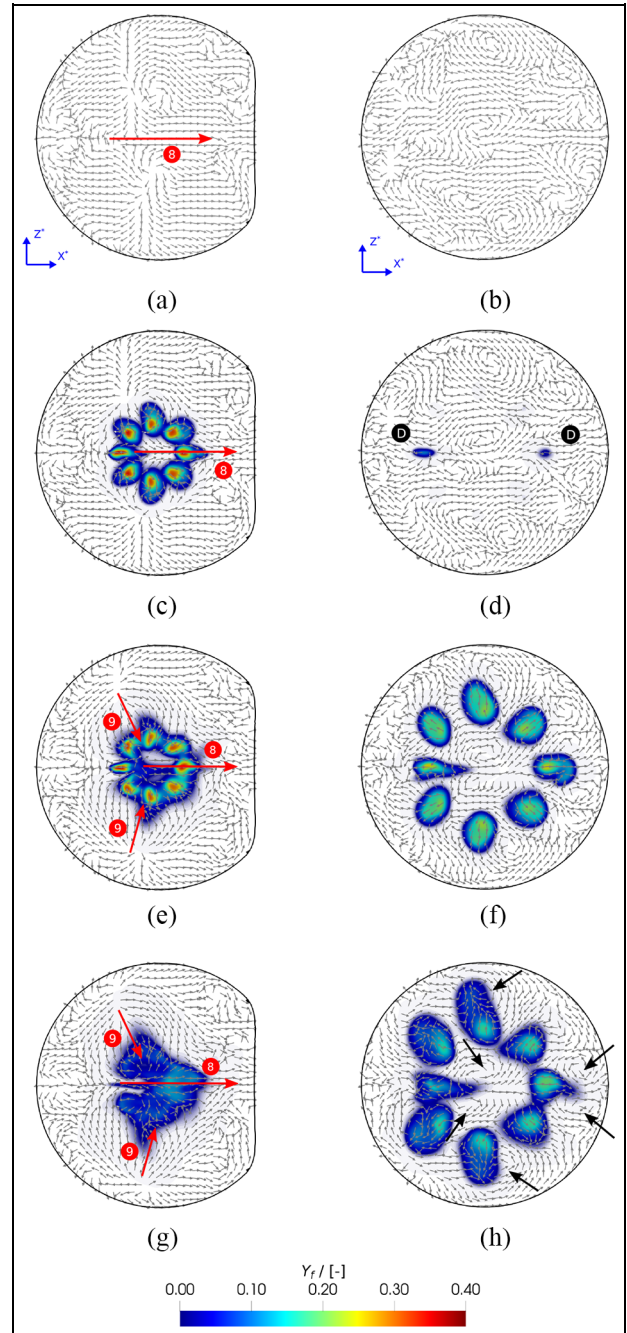

Figure 25. Velocity fields and iso-octane vapor mass fraction in the transverse plane at 15 mm (left column) and at 30 mm (right column) from the injector tip during the injection in the engine simulation. The ESOI is set up at 270° beforeTDC: (a and b) 1.25° after ESOI ≈ −46.6 μs after SOI, valve lift = 9.22 mm, (c and d) 3.25° after ESOI ≈ 370.1 μs after SOI, valve lift = 9.27 mm, (e and f) 5.0° after ESOI ≈ 734.7 μs after SOI, valve lift = 9.31 mm, and (g and h) 6.75° after ESOI ≈ 1099.2 μs after SOI, valve lift = 9.35 mm.

fuel region; the same phenomenon was observed in the section on "Spray-Flow Interaction."

It can be concluded that the vortex visible on the frontal plane, which represents the recirculation zone observable in CVC, is protected by the strong intake flow thanks to the intake valves. These strong vortices
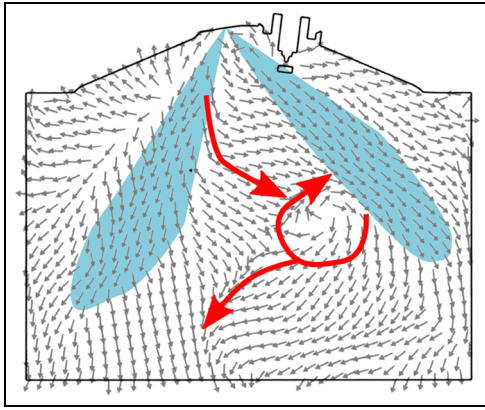
Figure 26. Phenomenological model of the interaction between Spray G and engines in the tumble plane. During the injection, a vortex is formed on the tip of the plume, directed toward the exhaust valves; this vortex generates an upward velocity which counteracts the downward velocity induced by the intake flow.
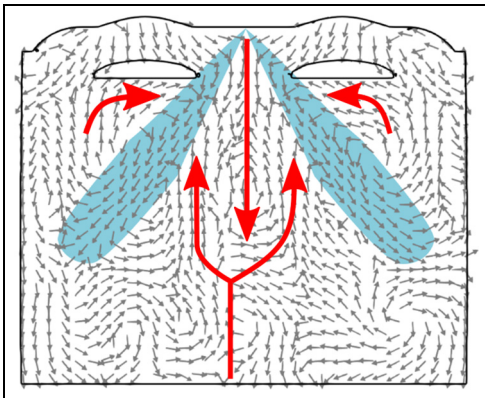

Figure 27. Phenomenological model of the interaction between Spray G and engines in the frontal plane. The vortices generated by the valves and by the spray interact together, increasing the air entrainment and enhancing the upward velocities which help spray stabilization, counteracting the intake flow. Furthermore, the intake valves prevents the blowout of these structures.

increase the dilution of the plumes outside the tumble plane and reduce the spray penetration as a consequence. Moreover, the upward flows beneath the valves play a role in the spray's dilution and stability.

Inter-plume interaction

In this section, the interaction between different plumes is investigated. Transverse cross-sections show the airflow between the plumes and highlight the inter-plume and plume-flow interactions. This plane is also interesting because in a static chamber a symmetric multi-hole spray exhibits a symmetrical flow distribution around the plumes.

Figure 25 shows the velocity field and iso-octane vapor mass fraction at a distance of 15 mm (left column) and 30 mm (right column) from the spray tip. Figure 25(a) and (c) show the flow directed from the intake side to the exhaust side (labeled "8"). This plays a role in the asymmetric spray evolution, as discussed before. In Figure 25(e) and (g) it can be seen that a major role in the spray dilution is played by the airflow from the lateral side of the spray (red arrow marked "9"), consistent with the mechanism explained in the "Spray-Valve Interaction" section.

Another phenomenon visible in Figure 25(g) is the merging of the upper fuel cloud into one distinct structure. This is triggered by the strong air entrainment from the side, with the mechanism described above, and the intake flow that drives the underflow plume toward the exhaust side. Thus, the spray behaves like that from horseshoe multi-hole injectors, with strong air entrainment from the side (labeled "8"). It is important to remember that horseshoe multi-hole injectors are known to have higher mixing ratios than a symmetrical geometry.[16] Although there is a lot of inter-plume interaction at a distance of 15 mm from the injector tip, at 30 mm the plumes are always separated.

In Figure 25(d), the tips of the plumes on the tumble plane are visible (labeled "D"), showing that these plumes penetrates further than others. This is because of the lower air dilution of tumble plumes compared to other plumes; it is also visible in Figure 25(f) and (h)

Figure 25(h) shows that all the plumes are asymmetric, particularly where recirculation vortices are visible (indicated by the black arrows). It can be concluded that the three-dimensional intake flow interacts with the engine walls leading to an in-cylinder flow characterized by several coherent structures. These structures interact with the spray, playing a relevant role in the spray asymmetry.

Conclusions

This work provides a comprehensive experimental and numerical analysis of the main phenomena typical of a multi-hole, early injection event under both constant-volume chamber (CVC) and DISI engine conditions. The ECN Spray G injector geometry was considered for both investigations and there was a particular focus on the interaction between the spray plumes and the in-cylinder charge motion characterized by a tumble flow structure. For both vessel and engine simulations the spray was numerically investigated by means of a dedicated model combining a dynamic KHRT approach originally introduced by Nagaoka and Kawamura[33] for secondary breakup and a Pilch–Erdman,[34] multi-motion regime mechanism for managing the atomization phase.

The aim of this unified model was to increase the accuracy of atomization and secondary breakup computations for multi-hole, GDI sprays characterized by low-evaporating conditions while providing a setup which could minimize required calibration and tuning

activities. The model was validated in the static chamber by testing the G3 operating condition according to the ECN Guidelines. The results were assessed in terms of the liquid and vapor penetration, axial PLV profiles, PLV maps for overall spray morphology, and average SMD compared with state-of-the-art experimental data available in the ECN community.

Bespoke experimental and numerical investigations were then carried out on the Darmstadt optical engine coupled with the Spray G injector geometry. The results were compared in terms of the spray liquid penetration, angle, asymmetry, and morphology. The gas velocity on the tumble plane before and after the injection event was also taken into account in the proposed analysis. Finally, the gas velocities and fuel distribution were respectively analyzed on tumble, frontal, and transverse planes with the aim of focusing on the interaction between the spray and in-cylinder flow during the injection process.

From the proposed analysis it can be concluded that:

- Results for the CVC spray simulation demonstrated good agreements with available experimental data. The adopted spray model provided accurate modeling of a low-evaporating GDI spray while not requiring specific tuning of the main parameters.
- The modeling approach was then employed in the engine simulation without parameter changes, yielding good agreement with experimental measurements in terms of the computed plume morphology. Particularly, a strong spray asymmetry was visible, caused by the intake flow directed toward the exhaust valve, while the spray angle was in accordance with experimental measurements.
- No spray collapse was observed either in the experiments or in the simulation.
- The values for the gas velocities on the tumble plane before and after the injection was similar, therefore it can be stated that the spray has no substantial effect on the flow field in the later stages.
- Considerable interaction between the flow and spray during the injection process was observed.
- The interaction of the spray with the in-cylinder charge motion and the engine walls induces an upward flow which helps slow down the closing of the spray angle.
- The interaction between the spray and the intake flow generates a vortex; this induces an upward flow that supports spray stabilization, as reported in Figure 26.
- On the frontal plane it can be observed that the upward flows below the valve plates, additionally reinforced by the tumble vortex, play a role in stabilizing the spray; a second set of vortexes located on the outer side of the spray are protected from the energetic intake flow by the intake valve and guided toward the spray; the combination of these phenomena explains the higher dilution and the lower penetration of the plumes outside the tumble plane. A sketch of the phenomenological model of these effects is shown in Figure 27.
- On the transverse plane near the injector tip the side radial inflow has a major role in spray dilution; the strong flow from the intake valves induces the collapse of the spray near the injector tip, leading to a spray shape similar to that of horseshoe multi-hole injectors; asymmetries in the plumes are observed and can be explained by the vortexes which are generated by the interaction between the spray and the in-cylinder flow.

ORCID iDs

Andrea Pati https://orcid.org/0000-0003-4279-2133
Davide Paredi https://orcid.org/0000-0003-4915-2606
Cooper Welch https://orcid.org/0000-0001-9067-9405
Marius Schmidt https://orcid.org/0000-0002-5424-1251
Christopher Geschwindner https://orcid.org/0000-0001-7869-2682
Tommaso Lucchini https://orcid.org/0000-0001-7677-8087
Gianluca D'Errico https://orcid.org/0000-0001-5248-7242
Christian Hasse https://orcid.org/0000-0001-9333-0911

References

1. Zhao F, Lai MC and Harrington DL. Automotive spark-ignited direct-injection gasoline engines. *Prog Energy Combust Sci* 1999; 25(5): 437–562.
2. Lake TH, Stokes J, Whitaker PA and Crump JV. Comparison of direct injection gasoline combustion systems. *SAE Trans* 1998; 107: 246–257.
3. Wirth M, Piock WF, Fraidl GK, Schoeggl P and Winklhofer E. Gasoline di engines: the complete system approach by interaction of advanced development tools. SAE technical paper 980492, 1998.
4. Moreira AL, Moita AS and Panão MR. Advances and challenges in explaining fuel spray impingement: how much of single droplet impact research is useful? *Prog Energy Combust Sci* 2010; 36(5): 554–580.
5. Han Z, Reitz RD, Claybaker PJ, Rutland CJ, Yang J and Anderson RW. Modeling the effects of intake flow structures on fuel/air mixing in a direct-injected spark-ignition engine. SAE technical paper 961192, 1996.

6. Han Z, Reitz RD, Yang J and Anderson RW. Effects of injection timing on air-fuel mixing in a direct-injection spark-ignition engine. SAE technical paper 970625, 1997.

7. Stanglmaier RH, Hall MJ and Matthews RD. Fuel-spray/charge-motion interaction within the cylinder of a direct-injected, 4-valve, SI engine. SAE technical papers 980155, 1998.

8. Alger T, Hall M and Ronald M. Fuel spray dynamics and fuel vapor concentration near the spark plug in a direct-injected 4-valve SI engine. SAE technical paper 1999-01-0497, 1999.

9. Alexander P, Begg S, Heikal M, Li G and Gold M. Air-flow and fuel spray interaction in a gasoline di engine. SAE technical paper 2005-01-2104, 2005.

10. Yi J, Han Z, Yang J, Anderson R, Trigui N and Boussarsar R. Modeling of the interaction of intake flow and fuel spray in DISI engines. SAE technical papers 2000-01-0656, 2000.

11. Mitroglou N, Nouri JM, Gavaises M and Arcoumanis C. Spray characteristics of a multi-hole injector for direct-injection gasoline engines. *Int J Engine Res* 2006; 7(3): 255–270.

12. Wirth M, Zimmermann D, Friedfeldt R, et al. A cost optimised gasoline spray guided direct injection system for improved fuel economy. In: *Seminar on fuel economy and engine downsizing. IMechE*, 2004. London, UK. 13 May 2004.

13. Preussner C, Döring C, Fehler S and Kampmann S. GDI: Interaction between mixture preparation, combustion system and injector performance. SAE technical paper 980498, 1998.

14. Mitroglou N, Arcoumanis C, Mori K and Motoyama Y. Mixture distribution in a multi-valve twin-spark ignition engine equipped with high-pressure multi-hole injectors. *J Phys Conf Ser* 2006; 45: 46–58.

15. Kim SJ, Kim YN and Lee JH. Analysis of the in-cylinder flow, mixture formation and combustion processes in a spray-guided GDI engine. SAE technical paper 2008-01-0142, 2008.

16. Dahlander P and Lindgren R. Multi-hole injectors for DISI engines: nozzle hole configuration influence on spray formation. *SAE Int J Engines* 2008; 1(1): 115–128.

17. Gutierrez L, Mansfield AB, Fatouraie M, et al. Effects of engine speed on spray behaviors of the engine combustion network "Spray G" gasoline injector. SAE technical paper 2018-01-0305, 2018.

18. Geschwindner C, Kranz P, Welch C, et al. Analysis of the interaction of Spray G and in-cylinder flow in two optical engines for late gasoline direct injection. *Int J Engine Res* 2020; 21: 169–184.

19. Stiehl R, Schorr J, Krüger C, Dreizler A and Böhm B. In-cylinder flow and fuel spray interactions in a stratified spray-guided gasoline engine investigated by high-speed laser imaging techniques. *Flow Turbul Combust* 2013; 91: 431–450.

20. Pati A, Paredi D, Lucchini T and Hasse C. CFD modeling of gas-fuel interaction and mixture formation in a gasoline direct-injection engine coupled with the ECN Spray G injector. SAE technical paper 2020-01-0327, 2020.

21. Reitz R. Modeling atomization processes in high pressure vaporizing sprays. *Atomization Spray Technol* 1987; 3: 309–337.

22. Vervisch L. ERCOFTAC best practice guidelines "computational fluid dynamics of turbulent combustion", https://hal.archives-ouvertes.fr/hal-02420318 (2015, accessed on 25-Mar-2021).

23. Paredi D, Lucchini T, D'Errico G, Onorati A, Pickett L and Lacey J. Validation of a comprehensive computational fluid dynamics methodology to predict the direct injection process of gasoline sprays using Spray G experimental data. *Int J Engine Res* 2020; 21(1): 199–216.

24. Sphicas P, Pickett L, Skeen S, et al. A comparison of experimental and modeled velocity in gasoline direct-injection sprays with plume interaction and collapse. *SAE Int J Fuels Lubr* 2017; 10(1): 184–201.

25. Sphicas P, Pickett LM, Skeen SA and Frank JH. Inter-plume aerodynamics for gasoline spray collapse. *Int J Engine Res* 2018; 19(10): 1048–1067.

26. Engine Combustion Network. Gasoline spray combustion, https://ecn.sandia.gov/gasoline-spray-combustion/ (2015, accessed on 25-Mar-2021).

27. Baum E, Peterson B, Böhm B and Dreizler A. On the validation of les applied to internal combustion engine flows: part 1: comprehensive experimental database. *Flow Turbul Combust* 2014; 92(1–2): 269–297.

28. Engine Combustion Network. Spray G nominal Geometry, https://ecn.sandia.gov/gasoline-spray-combustion/computational-method/mesh-and-geometry/(2015, accessed on 25-Mar-2021).

29. Engine Combustion Network. Primary Spray G datasets, https://ecn.sandia.gov/gasoline-spray-combustion/target-condition/primary-spray-g-datasets/ (2015, accessed on 25-Mar-2021).

30. Amsden A, O'Rourke P and Butler T. *KIVA-II: a computer program for chemically reactive flows with sprays 1989.* Los Alamos, NM: Los Alamos National Lab, 1989.

31. Grover R. Topic 8: internal and near nozzle flow modeling spray G, https://ecn.sandia.gov/wp-content/uploads/2016/08/ECN4Grover.mov(2016, accessed on 25-Mar-2021).

32. Paredi D. *CFD modeling and validation of spray evolution in gasoline direct injection engines.* Politecnico di Milano, Department of energy, doctoral programme in energy and nuclear science and technology, 2020. Milan, Italy.

33. Nagaoka M and Kawamura K. A Deforming Droplet Model for Fuel Spray in Direct-Injection Gasoline Engines. SAE technical paper 2001-03-05, 2001.

34. Pilch M and Erdman CA. Use of breakup time data and velocity history data to predict the maximum size of stable fragments for acceleration-induced breakup of a liquid drop. *Int J Multiphase Flow* 1987; 13(6): 741–757.

35. Baumgarten C. *Mixture formation in internal combustion engines.* New York, NY: Springer Science & Business Media, 2006.

36. Paredi D, Lucchini T, D'Errico G, Onorati A, Pickett L and Lacey J. CFD modeling of spray evolution for spark-ignition, direct injection engines. In: *AIP conference proceedings*, 2019, vol. 2191, no. 1, p.020125. 11–13 Sep 2019. Modena, Italy.

37. Ranz WE and Marshall WR Jr. Evaporation from drops, Part I. *Chem Eng Prog* 1952; 48(3): 141–146.

38. Ranz WE and Marshall WR Jr. Evaporation from drops, Part II. *Chem Eng Prog* 1952; 48(4): 173–180.

39. Freudenhammer D, Peterson B, Ding CP, Boehm B and Grundmann S. The influence of cylinder head geometry variations on the volumetric intake flow captured by magnetic resonance velocimetry. *SAE Int J Engines* 2015; 8(4): 1826–1836.

40. Payri R, Salvador FJ, Martí-Aldaraví P and Vaquerizo D. ECN Spray G external spray visualization and spray collapse description through penetration and morphology analysis. *Appl Therm Eng* 2017; 112: 304–316.

41. Pope SB. An explanation of the turbulent round-jet/plane-jet anomaly. *AIAA J* 1978; 16: 279–281.

42. Engine Combustion Network. Spray G parametric variation, https://ecn.sandia.gov/gasoline-spray-combustion/target-condition/spray-g-parametric-variation/(2015, accessed on 25-Mar-2021).

43. Paredi D, Lucchini T, D'Errico G, et al. Combined experimental and numerical investigation of the ECN Spray G under different engine-like conditions. SAE technical paper 2018-01-0281, 2018.

44. Maes N, Dam N, Somers B, Lucchini T, D'Errico G and Hardy G. Experimental and numerical analyses of liquid and spray penetration under heavy-duty diesel engine conditions. *SAE Int J Fuel Lubricants* 2016; 9: 108–124.

45. Linstrom PJ and Mallard WG. The NIST chemistry webbook: a chemical data resource on the internet. *J Chem Eng Data* 2001; 46(5): 1059–1063.

46. McBride BJ. *Coefficients for calculating thermodynamic and transport properties of individual species*, vol. 4513. NASA Langley Research Center, Hampton, Virginia. USA. 1993.

47. Issa RI. Solution of the implicitly discretised fluid flow equations by operator-splitting. *J Comput Phys* 1986; 62(1): 40–65.

48. Lucchini T, Paredi D and Lacey J. Topic 10: evaporative Spray G (external, plume interaction, flash boiling). In: *ECN6 proceedings*, Valencia, 10–11 September 2018.

49. Engine Combustion Network. ECN6 workshop, https://ecn.sandia.gov/ecn-workshop/ecn6-workshop/ (2018, accessed on 25-Mar-2021).

50. Paredi D, Lucchini T, D'Errico G, Onorati A, Golini S and Rapetto N. Gas exchange and injection modeling of an advanced natural gas engine for heavy duty applications. SAE technical paper 2017-24-0026, 2017.

51. Lucchini T, D'Errico G, Onorati A, Bonandrini G, Venturoli L and Di Gioia R. Development of a CFD approach to model fuel-air mixing in gasoline direct-injection engines. SAE paper 2012-01-0146, 2012.

52. Lucchini T, Della Torre A, D'Errico G, Montenegro G, Fiocco M and Maghbouli A. Automatic mesh generation for CFD simulations of direct-injection engines. SAE paper 2015-01-0376, 2015.

53. Lucchini T, D'Errico G and Fiocco M. Multi-dimensional modeling of gas exchange and fuel-air mixing processes in a direct-injection, gas fueled engine. SAE paper 2011-24-0036, 2011.

54. Lucchini T, D'Errico G, Onorati A, Bonandrini G, Venturoli L and Di Gioia R. Development and application of a computational fluid dynamics methodology to predict fuel–air mixing and sources of soot formation in gasoline direct injection engines. *Int J Engine Res* 2014; 15(5): 581–596.

55. Yang X, Keum S and Kuo TW. Effect of valve opening/closing setup on computational fluid dynamics prediction of engine flows. *J Eng Gas Turbine Power* 2016; 138(8): 081503-1-16.

56. Welch C, Schmidt M, Keskinen K, et al. The effects of intake pressure on in-cylinder gas velocities in an optically accessible single-cylinder research engine. SAE technical paper 2020-01-0792, 2020.

57. Hammer J, Kufferath A and Wehmeier K. Modern GDI combustion systems with focus on fuel metering technology fulfilling future emission legislation 2011. In: *SIA conference: the spark ignition engine of the future*, Strasbourg, France, 30 November–1 December 2011.

58. Welss R, Bornschlegel S and Wensing M. Characterizing spray propagation of GDI injectors under crossflow conditions. SAE technical paper 2018-01-1696, 2018.